nature cancer

RESOURCE

https://doi.org/10.1038/s43018-019-0018-6

Discovering the anticancer potential of non-oncology drugs by systematic viability profiling

Steven M. Corsello[1,2,3], Rohith T. Nagari[1], Ryan D. Spangler[1], Jordan Rossen[1], Mustafa Kocak[1], Jordan G. Bryan[1,6], Ranad Humeidi[1], David Peck[1], Xiaoyun Wu[1], Andrew A. Tang[1], Vickie M. Wang[1], Samantha A. Bender[1], Evan Lemire[1], Rajiv Narayan[1], Philip Montgomery[1], Uri Ben-David[1,7], Colin W. Garvie[1], Yejia Chen[1], Matthew G. Rees[1], Nicholas J. Lyons[1], James M. McFarland[1], Bang T. Wong[1], Li Wang[1,8], Nancy Dumont[1], Patrick J. O'Hearn[1,9], Eric Stefan[1,10], John G. Doench[1], Caitlin N. Harrington[1], Heidi Greulich[1], Matthew Meyerson[1,2,3], Francisca Vazquez[1], Aravind Subramanian[1], Jennifer A. Roth[1], Joshua A. Bittker[1,11], Jesse S. Boehm[1], Christopher C. Mader[1,12], Aviad Tsherniak[1] and Todd R. Golub[1,3,4,5]*

Anticancer uses of non-oncology drugs have occasionally been found, but such discoveries have been serendipitous. We sought to create a public resource containing the growth-inhibitory activity of 4,518 drugs tested across 578 human cancer cell lines. We used PRISM (profiling relative inhibition simultaneously in mixtures), a molecular barcoding method, to screen drugs against cell lines in pools. An unexpectedly large number of non-oncology drugs selectively inhibited subsets of cancer cell lines in a manner predictable from the molecular features of the cell lines. Our findings include compounds that killed by inducing phosphodiesterase 3A-Schlafen 12 complex formation, vanadium-containing compounds whose killing depended on the sulfate transporter SLC26A2, the alcohol dependence drug disulfiram, which killed cells with low expression of metallothioneins, and the anti-inflammatory drug tepoxalin, which killed via the multidrug resistance protein ATP-binding cassette subfamily B member 1 (ABCB1). The PRISM drug repurposing resource (https://depmap.org/repurposing) is a starting point to develop new oncology therapeutics, and more rarely, for potential direct clinical translation.

The prospect of repurposing existing drugs for new clinical indications is alluring: rapid clinical translation can occur for drugs already proven safe in humans. In principle, existing drugs can also establish starting points for drug development when new targets of old drugs are discovered. To date, most oncology repurposing discoveries have been serendipitous; systematic, at-scale screening of the entire pharmacopoeia has not been feasible. The extent to which non-oncology drugs have potential as future cancer therapeutics is unknown.

However, recent efforts have demonstrated the power of large-scale cancer cell line screening—testing either many compounds across a limited number of cell lines (for example, the NCI-60 panel[1]) or a modest number of oncology compounds across many cell lines (for example, the Genomics of Drug Sensitivity in Cancer (GDSC) project at the Sanger Institute[2] and the Cancer Target Discovery and Development (CTD[2]) project at the Broad Institute[3]; Fig. 1a). The ideal study would involve screening many drugs (most of which are non-oncology drugs) across a large panel of genomically characterized cell lines to capture the molecular diversity of human cancer.

In this study, we report the feasibility of using the PRISM molecular barcoding and multiplexed screening method to test 4,518 existing drugs against 578 cancer cell lines. We find that non-oncology drugs have an unexpectedly high rate of anticancer activity. The sensitivity of cancer cell lines to many of these compounds can be predicted from the genomic features of the cell lines, thereby suggesting potentially relevant patient populations.

Results

Drug selection and PRISM profiling. To facilitate the screening of thousands of compounds across hundreds of cell lines, we used the PRISM method. Cancer cell lines are labeled with unique DNA sequences, thereby allowing barcoded cell lines to be pooled with relative barcode abundance serving as a surrogate for cellular viability[4] (Fig. 1b). We screened 578 adherent cell lines spanning 24 tumor types (Extended Data Fig. 1a and Supplementary Table 1).

We chose 4,518 drugs from the Drug Repurposing Hub[5] (https://www.broadinstitute.org/repurposing) and confirmed the identity and purity of all compounds to be greater than 75% pure by liquid chromatography–mass spectrometry (LC–MS) (Supplementary Table 2); 3,350 of the compounds (74%) are either approved for clinical use in the USA or Europe, or are in clinical development. The remaining 1,168 (26%) are tool compounds with known activities. Most compounds, 3,466 (77%), were non-oncology-related, with

---

[1]Broad Institute of MIT and Harvard, Cambridge, MA, USA. [2]Department of Medical Oncology, Dana-Farber Cancer Institute, Boston, MA, USA. [3]Harvard Medical School, Boston, MA, USA. [4]Department of Pediatric Oncology, Dana-Farber Cancer Institute, Boston, MA, USA. [5]Howard Hughes Medical Institute, Chevy Chase, MD, USA. [6]Present address: Duke University, Durham, NC, USA. [7]Present address: Department of Human Molecular Genetics and Biochemistry, Tel Aviv University, Tel Aviv, Israel. [8]Present address: 10x Genomics, Pleasanton, CA, USA. [9]Present address: Relay Therapeutics, Cambridge, MA, USA. [10]Present address: Biogen, Cambridge, MA, USA. [11]Present address: Vertex Pharmaceuticals, Boston, MA, USA. [12]Present address: Flatiron Health, New York, NY, USA. *e-mail: golub@broadinstitute.org

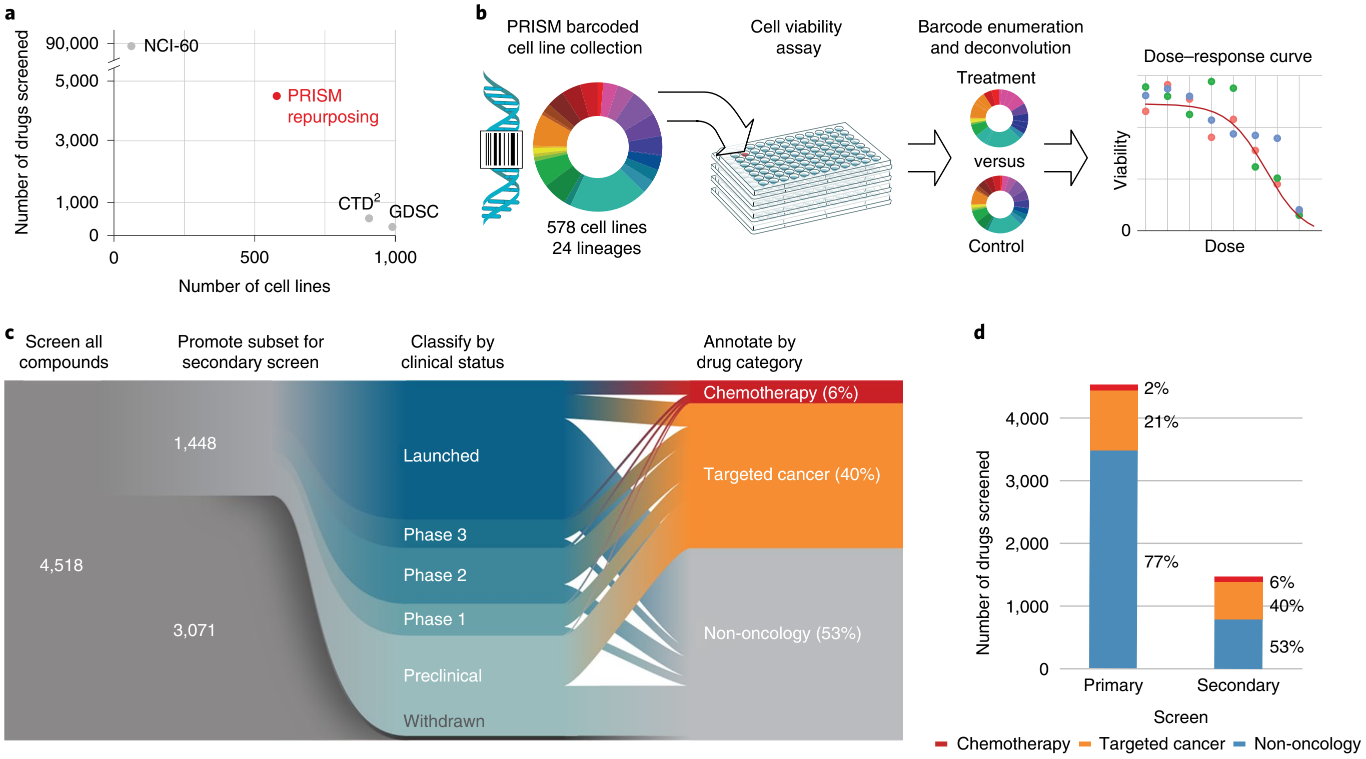

Fig. 1 | Generation of the PRISM Repurposing dataset. a, Dimensionality of publicly available pharmacogenomic drug screening experiments. The PRISM Repurposing dataset contains approximately tenfold more compounds than the CTD^2 and approximately tenfold more cell lines than the NCI-60. **b**, PRISM method overview. Barcoded cell lines are pooled in groups of 25 and treated with chemical perturbagens. Pools are lysed 5 d after perturbation and the relative abundance of mRNA barcodes is measured using MagPlex Microspheres (Luminex) to estimate cell viability. **c**, Repurposing screen workflow. A primary screen of 4,518 drugs was performed at 2.5 μM, followed by retesting of 1,448 active drugs at eight doses. Compounds were annotated as chemotherapy drugs, targeted cancer drugs or non-oncology drugs based on approved indications and prior clinical trial disease areas. **d**, Drug category representation in the primary and secondary screens. The secondary screen was enriched for chemotherapies and targeted cancer therapies.

the remaining compounds being either chemotherapeutics (2%) or targeted oncology agents (21%).

Screening results. We employed a 2-stage screening strategy whereby drugs were first screened in triplicate at a single dose (2.5 μM); 1,448 drugs screening positives were then rescreened in triplicate in an eight-point dose–response ranging from 10 μM to 610 pM (Fig. 1c and Supplementary Table 2). Interestingly, most active compounds (774 out of 1,448, 53%) were originally developed for non-oncology clinical indications (Fig. 1d). The primary and secondary screening datasets are available on the Cancer Dependency Map portal (https://depmap.org/repurposing) and figshare (https://doi.org/10.6084/m9.figshare.9393293; Extended Data Figs. 1–4). We compared the PRISM results to two gold standard datasets: GDSC (ref. [2]) and CTD^2 (ref. [3]). The three datasets shared 84 compounds tested on a median of 236 common cell lines, yielding 16,650 shared data points. The PRISM dataset had a similar degree of concordance to GDSC and CTD^2 (Pearson correlations of 0.60 and 0.61, respectively over all shared data points), as the GDSC and CTD^2 datasets had to each other (Pearson correlation 0.62) (Extended Data Fig. 5a). The three datasets remained similarly concordant when the analysis was restricted to data points showing evidence of anticancer activity (Extended Data Fig. 5b). We conclude that, despite differences in assay format, sources of compounds[5] and sources of cell lines[6], the PRISM Repurposing dataset is similarly robust compared to existing pharmacogenomic datasets.

At the level of individual compound dose–responses, we note that the PRISM Repurposing dataset tends to be somewhat noisier, with a higher standard error estimated from vehicle control measurements (Extended Data Fig. 5c and Extended Data Fig. 6a–c). This variation may be explained by a combination of longer assay duration, smaller number of cells assayed and/or variation attributable to growing cells in pools. However, such noise was not substantial enough to preclude the discovery of anticancer activities or their associated predictive biomarkers (see further on).

Landscape of non-oncology drug effects on cancer viability. We performed unsupervised clustering of compound viability profiles independent of their functional annotations using the uniform manifold approximation and projection (UMAP) method[7] (Fig. 2a; interactive plot available at https://depmap.org/repurposing). Compounds with similar mechanisms of action tended to cluster together, indicating that expected activities were recovered by the PRISM assay. Interestingly, while we expected to recover known mechanisms of action for cancer drugs, we also found clusters of functionally related noncancer drugs, such as vitamin D receptor agonists and 3-hydroxy-3-methylglutaryl-coenzyme A reductase inhibitors. Of note, some functionally related classes (for example, glucocorticoid receptor agonists) showed two or more distinct clusters, suggesting that biologically relevant substructures may exist within the dataset.

In general, chemotherapeutics killed the highest number of cell lines and non-oncology drugs the lowest, with targeted oncology drugs being intermediate (Fig. 2b). However, this pattern was highly dose dependent. At high doses, targeted agents lost their selectivity. Perhaps most interestingly, a subset of non-oncology drugs showed particularly potent activity: 91 drugs killed at least 1% of cell lines at a concentration of 625 nM or lower.

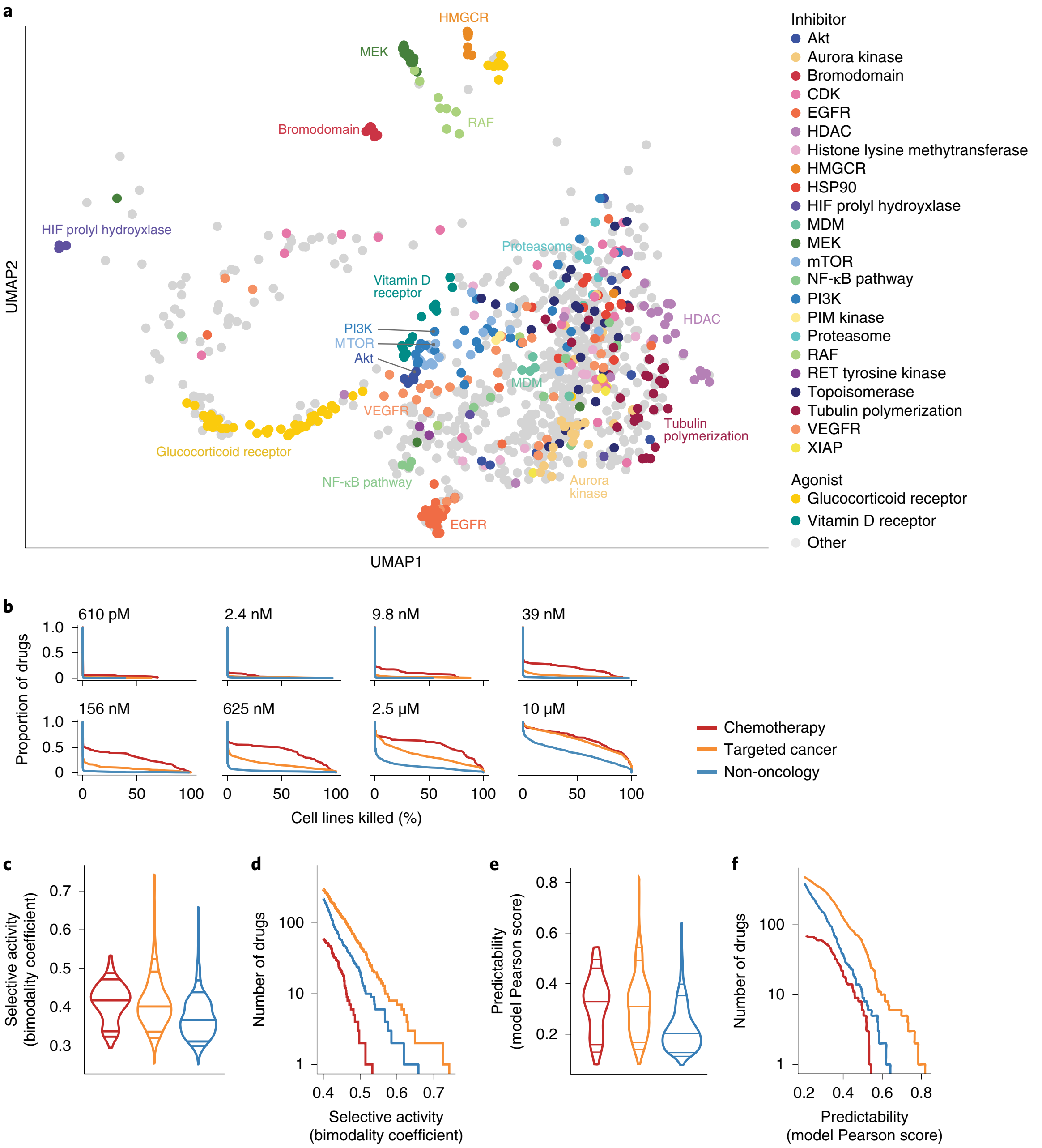

Fig. 2 | Drug response landscape of human cancer cell lines. a, Two-dimensional UMAP projection of 990 drug killing profiles by cosine similarity. Compounds with a shared annotated mechanism of action are labeled by color ($n = 640$ compounds). Compounds with an average Pearson correlation below 0.25 across three independent plates in one PRISM screen are not shown. **b**, Secondary screen drug activity by dose. Complementary cumulative distribution functions for the percentage of cell lines killed in each drug category (chemotherapy: $n = 90$ compounds; targeted cancer: $n = 584$ compounds; non-oncology: $n = 774$ compounds) at each dose of the secondary screen are shown. **c**, Selective compound activity by drug category. The global distribution of secondary screen bimodality coefficients is shown. Dose-wise bimodality coefficients are calculated from log fold change viability data; the maximum bimodality coefficient is shown for each compound. The violin plot lines correspond to the 5th, 10th, 50th, 90th and 95th quantiles. **d**, Most selective sensitivity profiles by drug category. The number of drugs (*y* axis) from each drug category with a bimodality coefficient at any dose greater than a given threshold (*x* axis) are shown. For visualization purposes, only drugs with a bimodality coefficient ≥ 0.4 are included. **e**, Predictability of compound activity by drug category (chemotherapy: $n = 90$; targeted cancer: $n = 584$; non-oncology: $n = 774$). The global distribution of secondary screen Pearson scores is shown. ATLANTIS random forest models are trained to predict PRISM log fold change values using cell line baseline omics and genomic perturbation profiles. The global distribution of secondary screen Pearson scores, defined as the correlation between actual and predicted PRISM profiles, is shown. The maximum Pearson score across all models is used for each compound. The violin plot lines correspond to the 5th, 10th, 50th, 90th and 95th quantiles. **f**, Most predictable sensitivity profiles by drug category. The number of drugs (*y* axis) from each drug category with a predictive model with a Pearson score greater than a given threshold (*x* axis) are shown. For visualization purposes, only drugs with a maximum Pearson score ≥ 0.2 are included.

To further investigate the therapeutic potential of non-oncology drugs, we computed the bimodality coefficient[8] of each compound's dose-wise viability profile (Extended Data Fig. 6d and Supplementary Table 3) and then calculated the maximum for each compound. While non-oncology drugs showed less bimodality than cancer drugs on average (Fig. 2c), the most selective compounds in

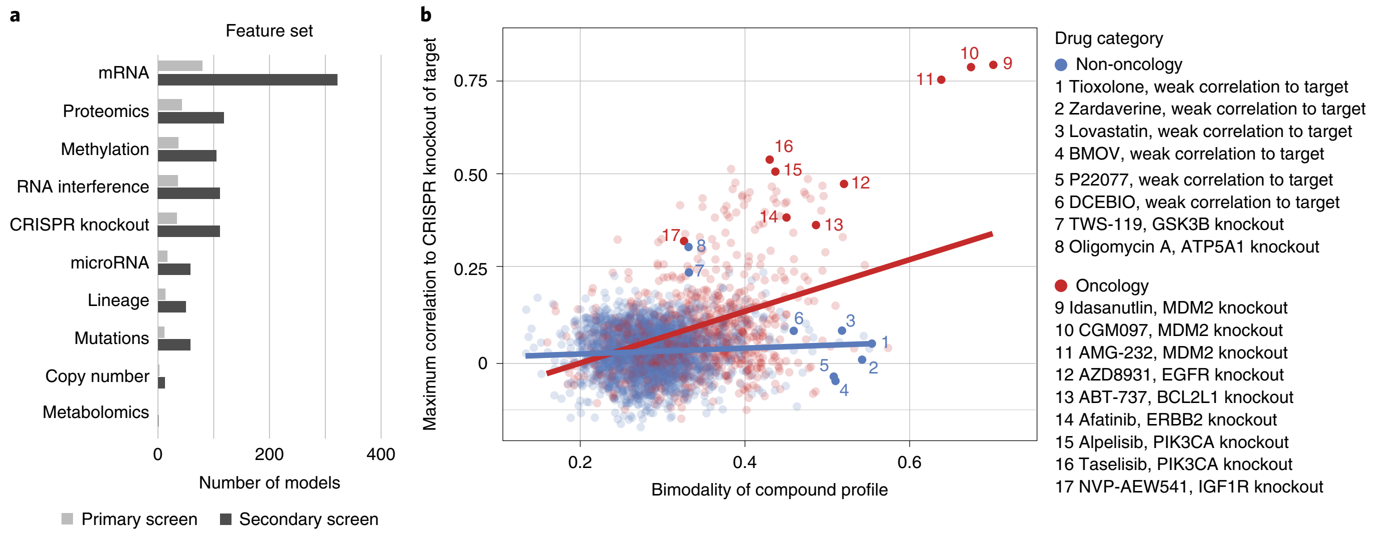

Fig. 3 | Predictors of drug sensitivity and comparison with genetic dependencies. **a**, Contributions of different genomic feature types to strong predictive models. A weighted set of genomic features predictive of drug activity was determined using the ATLANTIS implementation of random forests. Models with a Pearson score ≥ 0.4 are included. **b**, Relationship between the bimodality coefficient of the PRISM viability profile and correlation with the CRISPR knockout of the annotated gene target (oncology: $n = 885$ compounds; non-oncology: $n = 2{,}361$ compounds). Pearson correlations were computed between the primary screen log fold change profile of each compound and the DepMap Avana CRISPR–Cas9 gene knockout scores (CERES) of its annotated targets. For compounds with multiple target annotations, the maximum correlation is shown. Bimodality coefficients were calculated over cell lines shared by each compound and target shown. The linear regression lines are shown.

the dataset include non-oncology drugs (Fig. 2d). This provides further evidence that large-scale testing of noncancer drugs can reveal selective anticancer activity.

Predictive models of killing activity. We next addressed the extent to which cell-killing activity was predictable based on the genomic features of cell lines. For each drug, we used the random forest-based ATLANTIS algorithm[9], which employs the baseline molecular features (cell lineage; gene copy number; function-damaging, hotspot or missense mutations; DNA methylation levels; messenger RNA, microRNA, protein or metabolite abundance) and genetic dependencies (genome-scale CRISPR–Cas9 knockout or RNA interference) as inputs to the model[10–14]. Most of the highly predictable killing profiles came from targeted oncology drugs, compared to chemotherapeutics or non-oncology drugs (Fig. 2e and Supplementary Tables 4 and 5). This is not surprising, since targeted oncology drugs have been optimized for their selective killing of subtypes of cancer. More striking was the observation that a substantial number of non-oncology drugs had highly predictable patterns of killing (38 with a Pearson score > 0.4 in the secondary screen; Fig. 2f).

Interestingly, mRNA expression was by far the most predictive feature type compared to other categories of genomic information (Fig. 3a). This observation is consistent with the findings of other pharmacogenomic screens[15,16] as well as short hairpin RNA-based functional genomic screens[9]. By contrast, Iorio et al.[17] reported that mutation, not gene expression, was most predictive of drug response within a cancer type. Whether that is explained by their focus on known cancer drugs (for example, kinase inhibitors), as opposed to all classes of drugs analyzed in the present dataset, is to be determined. Importantly, only rarely (in 0.8% of cases) did the pattern of killing by active non-oncology drugs correlate with knockout or knockdown of the drug's intended target (versus 15.0% of active oncology drugs; Fig. 3b and Supplementary Table 6). This suggests that the unexpected anticancer activity of non-oncology drugs is most probably explained by a previously unrecognized mechanism of action.

In the primary screen, 195 non-oncology drugs had predictable killing with a Pearson score > 0.2, and 23 were predictable with a Pearson score > 0.4. This same phenomenon of highly predictable non-oncology drug killing was observed when predictability was plotted against the bimodality score (Fig. 4). The most predictable, bimodal non-oncology drugs (right plot; upper right-hand quadrant; Supplementary Tables 3 and 4) represent the drugs of greatest interest for future mechanistic follow-up. We describe four of these compounds in the sections that follow.

Inducers of PDE3A–SLFN12 protein–protein interaction. Among the genomic features most highly correlated with non-oncology drug activity was the expression of the gene *PDE3A*, whose expression correlated with killing by 11 structurally diverse compounds. These included the known phosphodiesterase 3A (PDE3A) inhibitors anagrelide and zardaverine, progesterone receptor agonists (including the nonsteroidal drug tanaproget), the kinase inhibitor AG-1296 and the potassium channel activator DCEBIO (Fig. 5a). This pattern of killing was of interest because of the recent report of cancer cytotoxicity occurring as a result of protein–protein interaction between PDE3A and the largely uncharacterized protein Schlafen 12 (SLFN12; (ref. [18])). We found that the structurally diverse compounds identified in the PRISM screen bound PDE3A in a thermal shift assay (Fig. 5b and Supplementary Table 7) and inhibited PDE3A enzymatic activity (Supplementary Table 7). Their cytotoxicity was completely rescuable by either *PDE3A* knockout or by competition with trequinsin, a potent PDE3A small-molecule inhibitor that does not induce PDE3A–SLFN12 interaction[18] (Fig. 5c). Importantly, PDE3A pull-down resulted in coimmunoprecipitation of V5-tagged SLFN12 following compound treatment, indicating that these compounds indeed induced PDE3A–SLFN12 protein–protein interaction (Fig. 5d). We consistently observed that, while complex formation predicts compound sensitivity, the strength of the PDE3A–SLFN12 interaction does not directly correlate with HeLa cell line half maximal inhibitory concentration (IC$_{50}$; Fig. 5d and Supplementary Table 7). Taken together, the PRISM results show that an unexpectedly large number of structurally

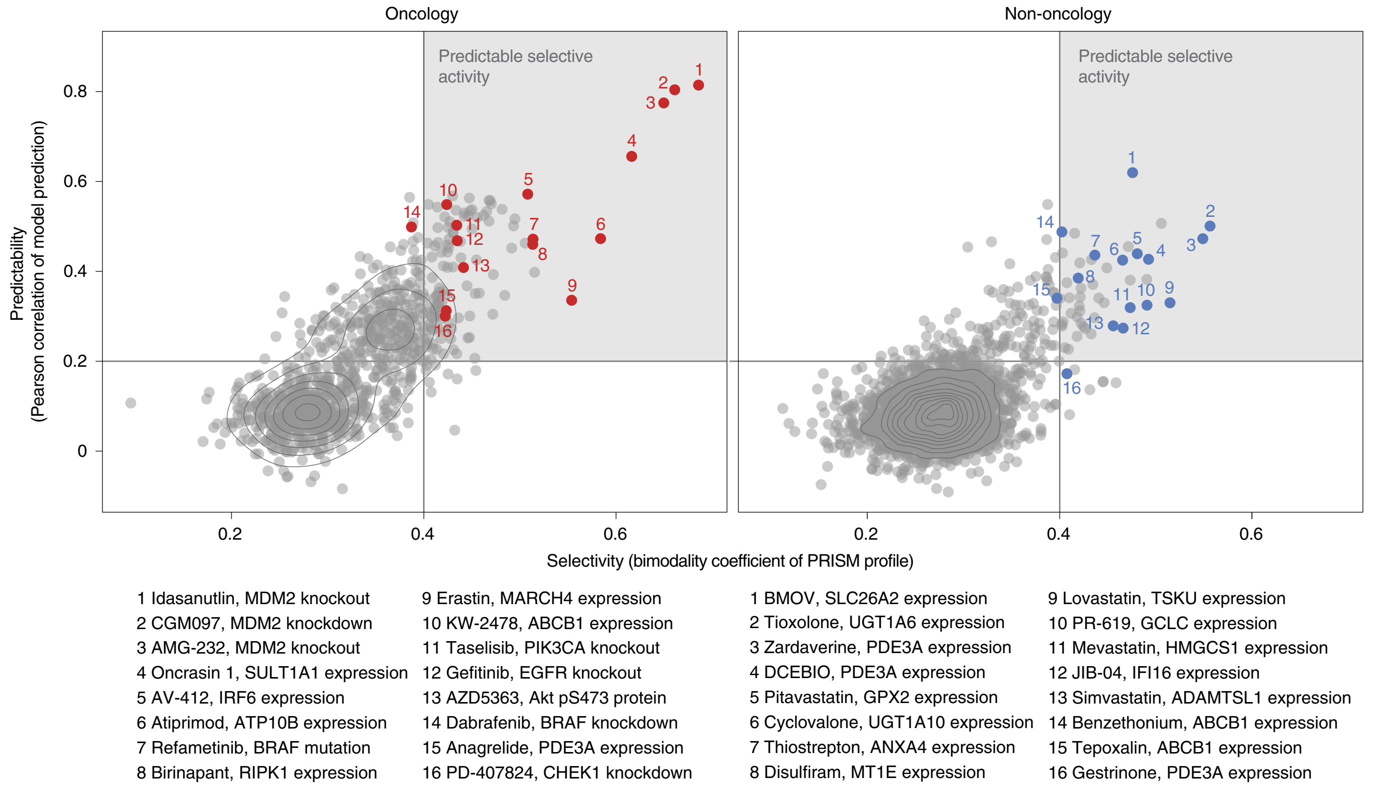

Fig. 4 | Predictive biomarker discovery using the PRISM Repurposing dataset. Prioritization of compounds based on strength of predictive models (Pearson score) and cell line selectivity (bimodality coefficient). Both known oncology ($n = 997$ compounds) and non-oncology ($n = 3{,}443$ compounds) sets contain compounds with high selectivity and predictability (strong model performance; upper right quadrant).

diverse non-oncology drugs kill PDE3A-expressing cancer cells by stabilizing the PDE3A–SLFN12 interaction. While these compounds have limited potency, they may prove useful as starting points for further medicinal chemistry optimization of this anticancer mechanism.

Predictive biomarkers of disulfiram activity. An intriguing observation was the association of killing by disulfiram, an inhibitor of acetaldehyde dehydrogenase used to treat alcohol dependence, and chromosome 16q copy number. Examination of the relevant region of 16q (ref. [19]) revealed that both copy number loss and low expression of the metallothionein-encoding genes *MT1E* and *MT2A* were correlated with disulfiram-induced cell killing (Pearson correlations of 0.33 and 0.23, respectively across 560 lines; Fig. 6a). Disulfiram has been previously suggested as an anticancer agent[20] and at least one clinical trial has shown hints of efficacy in lung cancer when used in combination with chemotherapy[21]. In the absence of a predictive biomarker, the magnitude of clinical benefit did not warrant further clinical investigation.

Our finding that the metallothionein-encoding genes *MT1E* and *MT2A* on 16q are predictive of disulfiram activity is mechanistically plausible: disulfiram's activity is copper-dependent, and MT1E and MT2A are known metal-chelating proteins[22]. Consistent with this observation, *MT1E* and *MT2A* expression was also correlated with sensitivity to thiram and elesclomol, other copper-binding compounds[23,24]. In addition, disulfiram has been reported to induce metallothionein gene expression in prostate cancer cells[25].

To test the hypothesis that metallothionein expression regulates disulfiram's anticancer activity, we used the disulfiram-resistant glioma cell line SF295, which has an amplification of chromosome 16q and high metallothionein expression. To inhibit the expression of multiple metallothionein genes simultaneously, we knocked out the transcription factor MTF1, which is a known upstream regulator of metallothionein gene expression (Extended Data Fig. 7a; ref. [22]). Following MTF1 knockout, metallothionein genes were among the most downregulated as assessed by global mRNA sequencing (Extended Data Fig. 7b). As predicted, MTF1 knockout resulted in increased sensitivity of SF295 cells to disulfiram; this increased sensitivity could be completely reversed by the copper chelator tetrathiomolybdate (TTM; Fig. 6b). MTF1 knockout did not alter sensitivity to control bortezomib (Extended Data Fig. 7c). These results together suggest that 16q deletion is a potential predictive biomarker of disulfiram and other copper-dependent cytotoxic agents. This finding is clinically relevant because arm-level 16q loss is seen in many tumor types, most notably breast and ovarian cancers, where its prevalence is estimated at 55–65% and 55–76%, respectively[26–28].

Vanadium-containing compounds. The PRISM screen revealed a strong correlation between killing by the vanadium-containing drug bis(maltolato)oxovanadium(IV) (BMOV) and expression of the sulfate transporter *SLC26A2* (Pearson correlation −0.583, ATLANTIS Pearson score 0.620; Fig. 6c). Bioavailable vanadium-containing compounds, including BMOV and bis(ethylmaltolato)oxovanadium(IV) (BEOV), have been of interest for their ability to lower fasting blood glucose in animal models and in patients with diabetes[29,30]. SLC26A2 function has not been extensively studied, but loss-of-function mutations have been associated with connective tissue disorders[31,32]. In cancer, *SLC26A2* is broadly expressed at modest levels, with high expression in melanoma and uterine cancers[33].

The mechanistic relationship between BMOV and *SLC26A2* expression is not obvious. Arguing against BMOV being an inhibitor of SLC26A2 function, analysis of publicly available genome-wide CRISPR–Cas9 loss-of-function screens indicates that *SLC26A2*

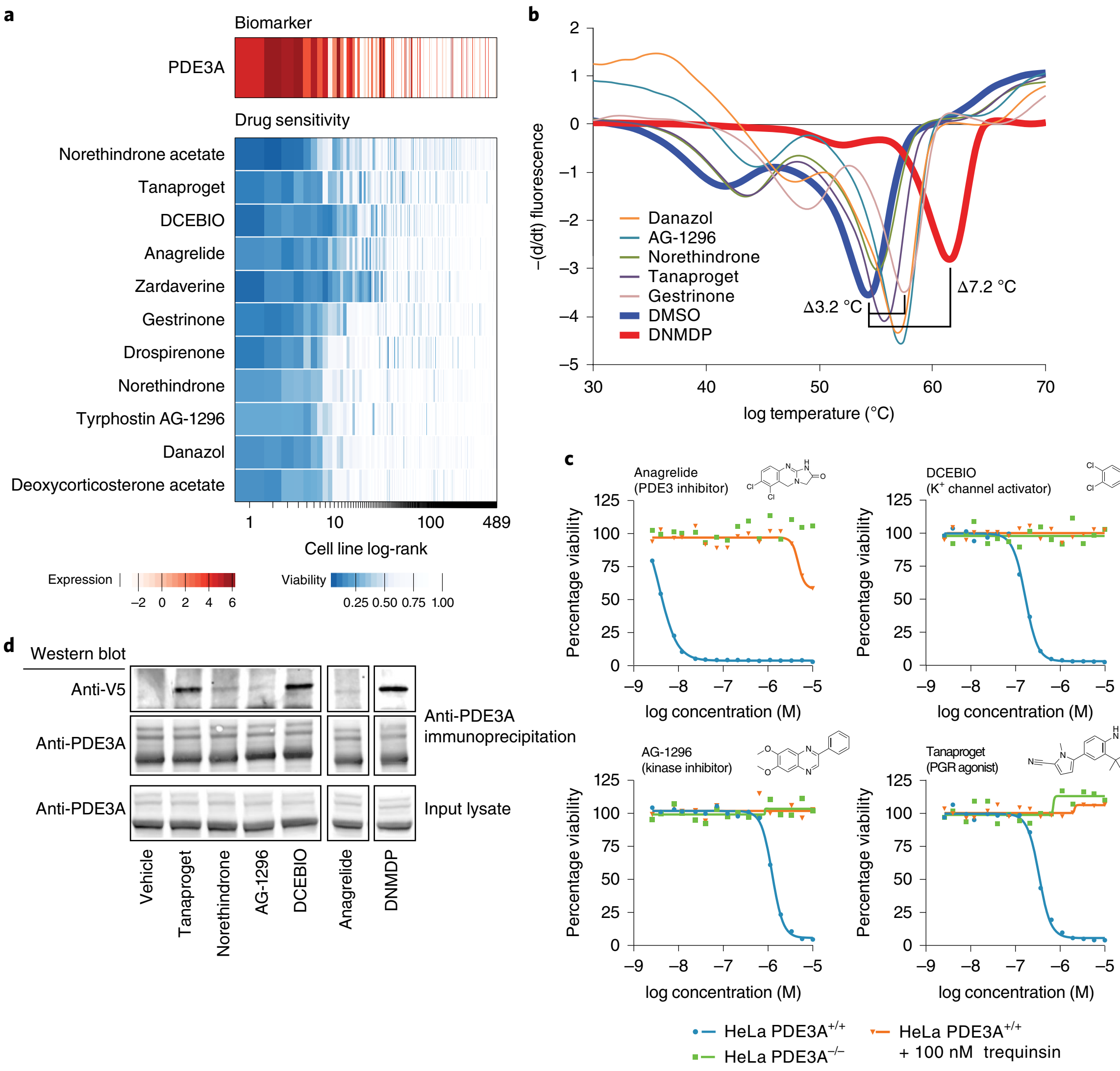

Fig. 5 | Multiple existing drugs selectively kill cancer cell lines by stimulating PDE3A–SLFN12 interaction. a, Drug sensitivity profiles associated with high *PDE3A* RNA expression ($n=489$ cell lines, $n=11$ compounds). *PDE3A* gene expression from CCLE RNA-seq data ($\log_2$ reads per kilobase of transcript per million mapped reads (RPKM), red) and cell line viability (blue) are indicated by color. Compounds where *PDE3A* expression was the top predictive biomarker by ATLANTIS from the PRISM 2.5 µM primary screen are shown. Cell lines are ranked by mean viability of the indicated compounds with a ceiling set at 1 (100%). **b**, Thermal shift assay performed with recombinant PDE3A. Stabilization of PDE3A protein was seen for a subset of hit compounds. DNMDP is included as an established positive control for strong PDE3A binding. Full ΔTm results are shown in Supplementary Table 7. The results are representative of two independent experiments. **c**, HeLa cell line dose–response curves with PDE3A genetic loss or pharmacological inhibition. Knockout of *PDE3A* was performed by CRISPR–Cas9. Parental HeLa cell killing was rescued by cotreatment with 100 nM of the noncytotoxic PDE3A inhibitor trequinsin. Mean viability across two independently treated wells in one experiment is shown. **d**, Coimmunoprecipitation of V5-tagged SLFN12. PDE3A-modulating compounds induce complex formation between PDE3A and SLFN12. Anti-V5 western blot using lysates from HeLa cells treated with the indicated compound at 10 µM for 8 h is shown. The anagrelide and DNMDP lanes were run on the same gel as all other samples and were cropped for figure purposes. The anagrelide and DNMDP results are consistent across three independent experiments. All other compounds were tested twice, with the exception of norethindrone (tested once with the expected results).

is not a cancer dependency (see https://depmap.org). Consistent with this, knockout of *SLC26A2* in the BMOV-sensitive cell line OVISE was tolerated (Extended Data Fig. 7d,e). However, *SLC26A2* knockout rendered OVISE cells resistant to both BMOV and BEOV, indicating that *SLC26A2* is not simply a biomarker of killing, but is required for compound activity (Fig. 6d). The cytotoxicity of other, structurally distinct vanadium-containing compounds was similarly rescued by *SLC26A2* knockout, suggesting that the vanadium oxide ion is responsible for the SLC26A2-dependent cytotoxicity of BMOV (Fig. 6e). It remains to be determined whether these compounds are substrates for the SLC26A2 transporter, interfere with sulfate ion homeostasis or confer a previously unknown function to SLC26A2.

Tepoxalin and multidrug resistance. Expression of metabolic enzymes or drug efflux pumps were among the most common predictive biomarkers of drug response in the PRISM screen. As expected, high mRNA expression of the gene encoding the ABCB1 transporter (also known as multidrug resistance protein 1 (MDR1) or p-glycoprotein 1) was the top predictor of resistance to numerous

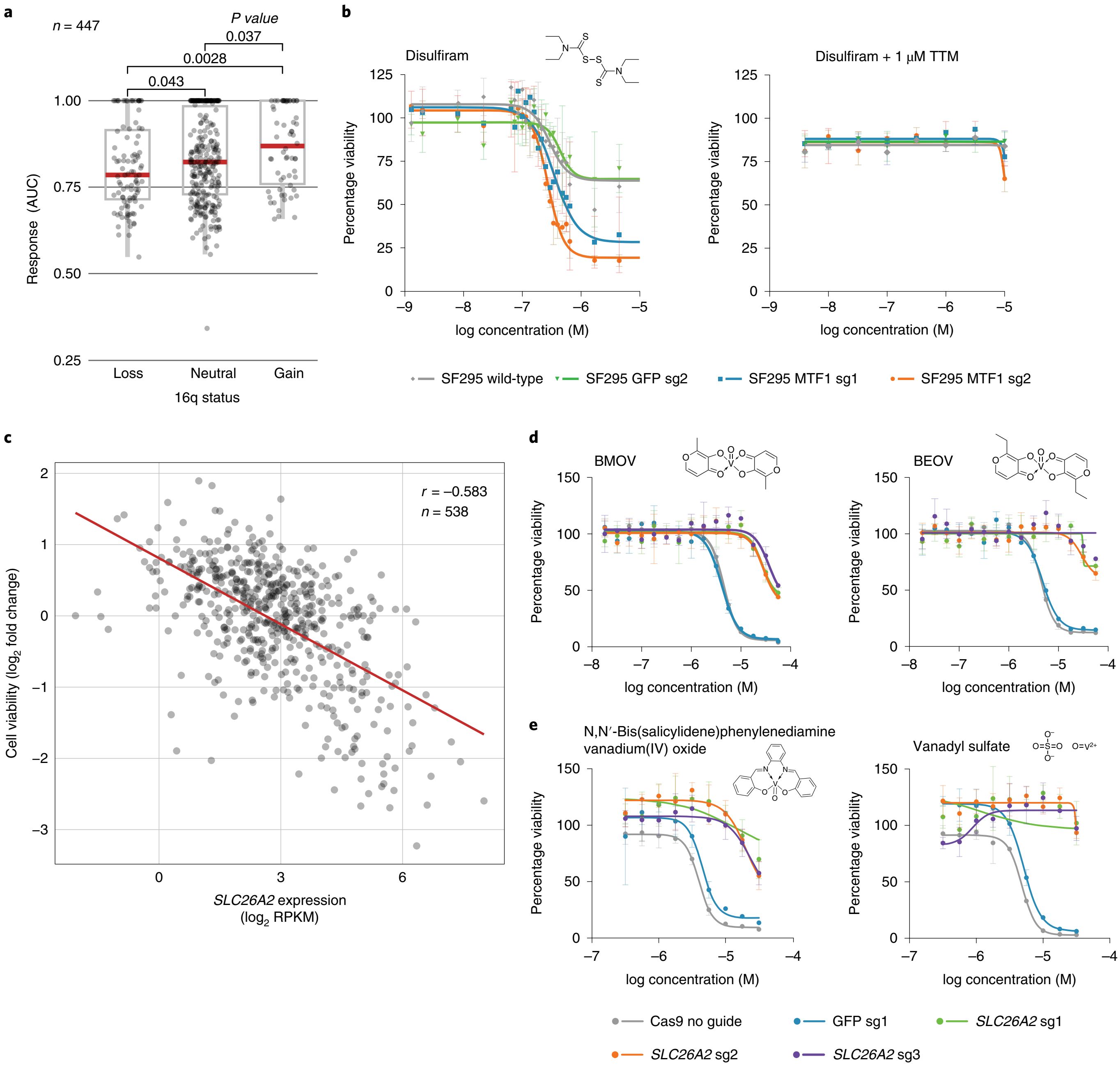

Fig. 6 | Anticancer activity of disulfiram and vanadium. a, Disulfiram sensitivity of PRN,N′-Bis(salicylidene)phenylenediamine vanadium(IV) oxideISM cell lines grouped by 16q copy number status ($n=447$ cell lines). PRISM secondary data are shown as AUCs. Arm-level copy number data were obtained using published The Cancer Genome Atlas methods and manually reviewed to ensure consistency with copy number at the 16q13 locus. Two-sided *P* values were calculated using the Wilcoxon signed-rank test between each pair of groups. The upper box limits, center lines and lower box limits correspond to the 75th, 50th and 25th percentiles, respectively. The whiskers extend from the box limits to the most extreme value up to 1.5 interquartile range from the median. All cell lines are depicted as points, regardless of outlier status. **b**, *MTF1* loss sensitizes to disulfiram. Drug sensitivity of SF295 cells with and without *MTF1* knockout, with sgRNA against GFP included as a nontargeting control. Cotreatment with 1 μM TTM is included. Mean viability across three independently treated wells is shown, with the s.d. indicated by the error bars. **c**, Scatter plot of BMOV sensitivity versus *SLC26A2* gene expression ($n=538$ cell lines). Correlation between PRISM viability data at 2.5 μM and *SLC26A2* gene expression from CCLE RNA-seq ($\log_2$ RPKM) is shown. Pearson's *r* is shown. **d**, *SLC26A2* knockout confers resistance. Dose–response curves for BMOV and BEOV in OVISE cells with and without CRISPR–Cas9-mediated knockout of *SLC26A2*. sgRNA against GFP was included as a nontargeting control. Mean viability across three independently treated wells is shown with the s.d. indicated by the error bars. **e**, Dose–response curves for related vanadium-containing compounds, N,N′-Bis(salicylidene)-o-phenylenediamine vanadium(IV) oxide and vanadyl sulfate, in OVISE cells with and without *SLC26A2* knockout. Mean viability across three independently treated wells is shown, with the s.d. indicated by the error bars.

oncology drugs, including taxanes (docetaxel and paclitaxel), vinca alkaloids (vincristine and vinorelbine) and proteasome inhibitors (carfilzomib) (Fig. 7a).

An unexpected finding, however, was that a single drug, tepoxalin, had the opposite relationship to ABCB1: high *ABCB1* expression predicted sensitivity to tepoxalin. Tepoxalin is a dual cyclooxygenase

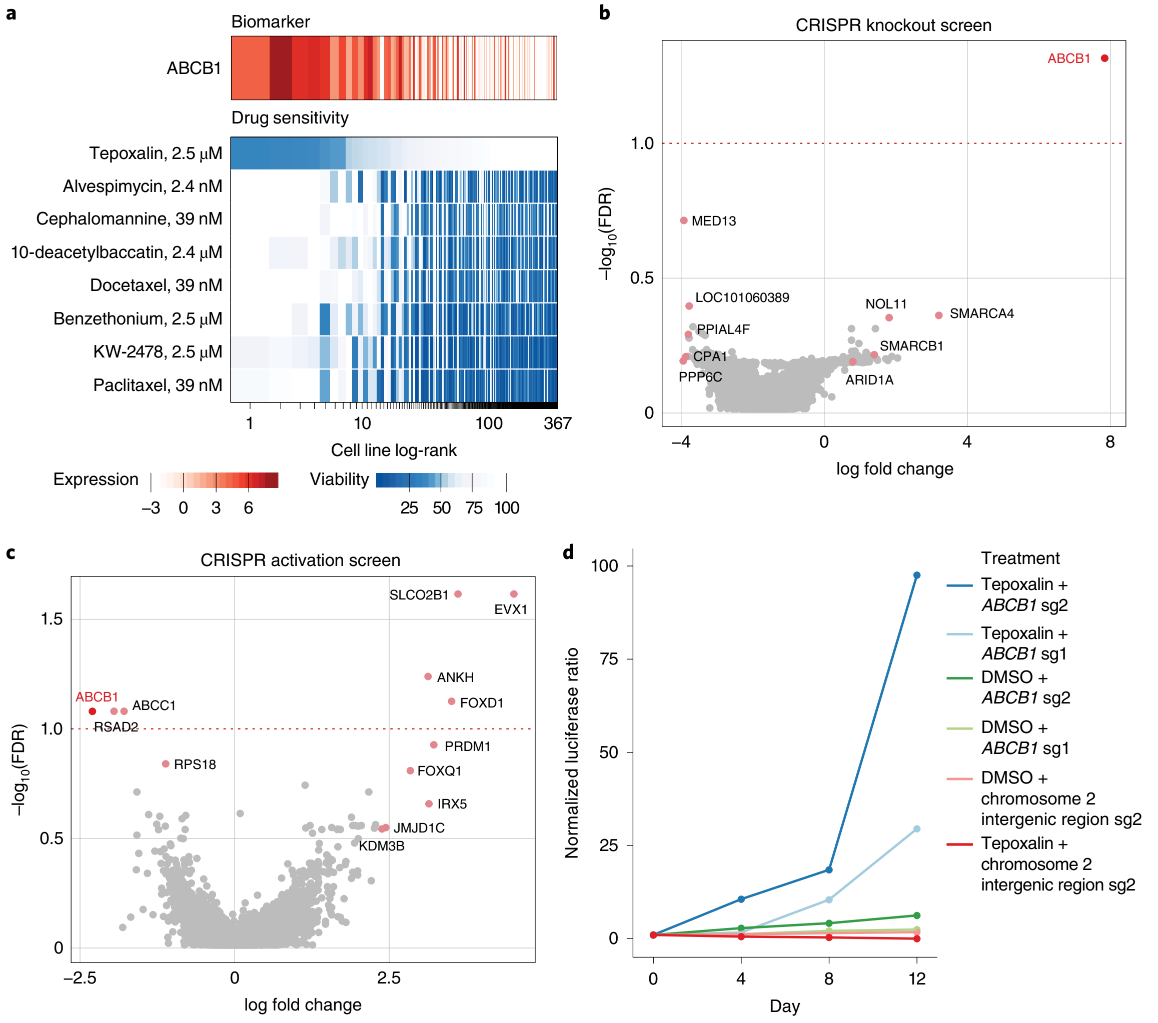

Fig. 7 | Tepoxalin is active against ABCB1-high cancer cell lines via an ABCB1-mediated mechanism. a, Drug sensitivity profiles of tepoxalin and seven additional compounds where *ABCB1* RNA expression was the top predictive genomic feature of the PRISM activity profile ($n = 489$ cell lines). Tepoxalin was the only compound tested where high *ABCB1* expression was associated with sensitivity rather than resistance to tepoxalin. Cell line viability is depicted with *ABCB1* gene expression from CCLE RNA-seq $\log_2$ RPKM data. Cell lines are ranked by mean viability with the ceiling at 100%. **b**, *ABCB1* knockout is the top hit that rescues tepoxalin activity in a genome-wide CRISPR–Cas9 gene knockout screen. LS1034-Cas9 cells (pXPR_311) were infected with the Brunello sgRNA library, selected with puromycin and treated with 16 µM tepoxalin versus vehicle control with two replicates in independent flasks. Cells were passaged every 3–4 d over a 30-d period. Two-sided *P* values were computed using MAGeCK-MLE and are shown versus gene-level log fold changes. **c**, *ABCB1* overexpression sensitizes to tepoxalin activity in a genome-wide CRISPR-dCas9 gene activation screen. LS1034-dCas9 cells (pXPR_109) were infected with the Calabrese sgRNA library, selected with puromycin and treated with 16 µM tepoxalin versus vehicle control with two replicates in independent flasks. Cells were passaged every 3–4 d over a 14-d period. Two-sided *P* values were computed using MAGeCK-MLE and are shown versus gene-level log fold changes. **d**, Tepoxalin cellular competition assay after *ABCB1* knockout. LS1034-Cas9 cells (pXPR_311) were stably infected with firefly luciferase; parental LS1034 cells (without Cas9) were stably infected with *Renilla* luciferase. Cells were mixed in a 1:1 ratio and infected with the indicated sgRNA construct against *ABCB1* or an intergenic region on chromosome 2 (negative control). After puromycin selection, cell mixtures were treated with 16 µM tepoxalin. The firefly:*Renilla* luminescence ratio is plotted as the log fold change over time. The mean of three technical replicates is shown and the results are representative of three independent experiments.

and 5-lipoxygenase inhibitor that is Food and Drug Administration-approved for the treatment of osteoarthritis in dogs[34,35]. Because more than 100 other cyclooxygenase and/or 5-lipoxygenase inhibitors were also tested in our PRISM screen, we asked whether they shared the *ABCB1*-associated killing effect. Strikingly, none of them did, suggesting that tepoxalin's killing was most probably explained by an off-target mechanism. Consistent with this hypothesis, tepoxalin's killing activity was not correlated with the genetic knockout profiles of its known targets *PTGS1*, *PTGS2* and *ALOX5*.

To gain insight into the mechanism by which tepoxalin selectively inhibits cancer cells, we performed a genome-wide CRISPR–Cas9 modifier screen to identify the genes required for tepoxalin-mediated activity. LS1034 colorectal cancer cells have high levels of *ABCB1* expression and are inhibited by tepoxalin with an IC_{50} of 3.8 µM. Cas9-expressing LS1034 cells were infected with a pooled library containing 76,441 single guide RNAs (sgRNAs) targeting 19,114 genes and treated with 16 µM tepoxalin (or vehicle control) for 28 d. Remarkably, the gene knockout most enriched in tepoxalin-resistant cells was *ABCB1* itself (Fig. 7b). Other resistance hits included multiple components of the SWI/SNF complex (*SMARCA4*, *SMARCB1* and *ARID1A*), which has been previously implicated in the regulation of *ABCB1* gene expression[36].

To complement the CRISPR–Cas9 loss-of-function screen, we performed a genome-wide CRISPR activation screen to identify genes whose overexpression was selected against in the setting of tepoxalin treatment. The gene showing the most negative selection was also *ABCB1*, indicating that its overexpression sensitizes cells to tepoxalin (Fig. 7c). Consistent with these findings, cellular competition and dose–response assays revealed strong selection for tepoxalin-treated *ABCB1*-null cells compared to wild-type cells (Fig. 7d, Extended Data Fig. 7f–h and Supplementary Table 8). Overexpression of *ABCB1* in a low-expressing, tepoxalin-insensitive cell line resulted in increased drug sensitivity (Extended Data Fig. 8a,b). Furthermore, potent ABCB1 small-molecule inhibitors did not phenocopy tepoxalin in the PRISM assay and in fact antagonized tepoxalin-induced killing, suggesting that ABCB1 inhibition alone does not explain tepoxalin's anticancer activity (Extended Data Fig. 8c,d).

Given that *ABCB1* encodes a drug transporter, we next asked whether ABCB1 expression affected intracellular concentrations of tepoxalin. However, LC–MS experiments indicated that intracellular concentrations of tepoxalin were unaffected by levels of ABCB1 expression or by ABCB1 small-molecule inhibition (Extended Data Fig. 8e). Tepoxalin is also known to be metabolized to a compound known as RWJ20142 by conversion of its hydroxamic acid to a carboxylic acid[37]. RWJ20142 is generated in the presence of serum but not saline or acetonitrile (Extended Data Fig. 8f). Unlike tepoxalin, RWJ20142 was not cell permeable and showed no inhibition of *ABCB1*-expressing cancer cells. Although tepoxalin inhibited ABCB1 at high concentrations (Extended Data Fig. 8g,h), our results indicate that tepoxalin does not kill cancer cells simply by inhibiting ABCB1 activity. Taken together, these results suggest that tepoxalin, but not its metabolite RWJ20142, inhibits *ABCB1* high-expressing cancer cells via an ABCB1-mediated mechanism that remains to be fully elucidated.

Discussion

We developed the PRISM Repurposing dataset as a large-scale resource containing the anticancer activity of non-oncology drugs. The PRISM screen recovered 49 non-oncology compounds with selective and predictive biomarker-associated anticancer activity (Pearson score > 0.2, bimodality coefficient > 0.4) and 103 with a less stringent bimodality coefficient cutoff (>0.35). Of note, six non-oncology compounds (Fig. 4) showed selective (bimodal) killing patterns, but their activity was unpredictable based on the baseline genomic features of the cell lines. It is possible that an expansion of the number of cell lines in the PRISM panel will help identify such biomarkers. Alternatively, killing might be explained by molecular features not yet measured in the cell lines.

It is conceivable that some non-oncology drugs could be brought directly to clinical trials for testing in cancer patients. However, before doing so, it is important to establish that the killing activity of such drugs is observed at concentrations that are achievable and tolerable in humans. Similarly, it is important to confirm that the predictive biomarkers identified in cell lines represent distinct populations of human tumors in vivo. It is probable that most of the observations described in this study will not be suitable for immediate testing in humans; either the biomarker hypothesis will require further refinement or the compounds themselves will require further optimization.

In contrast to immediate repositioning of existing drugs for new indications, the PRISM results reported in this study also represent starting points for new drug development. When the anticancer activity of a drug occurs via an off-target mechanism, it is probable that further optimization for this new target will result in more potent and selective drug candidates. We note that the use of cell-based screens such as PRISM allows for the discovery of previously unknown mechanisms of action that would be difficult to discover using conventional biochemical screening assays.

We initiated follow-up studies on four of the initial findings from the PRISM screen. In the case of disulfiram, we discovered a previously unrecognized biomarker (16q deletion) that predicts sensitivity. Future work will require extending such studies to the in vivo setting and determining whether sufficiently high disulfiram concentrations can be achieved to obtain anticancer effects. The accessibility of copper in different organs and cell types probably also modulates disulfiram's anticancer activity. Compounds with remarkable chemical diversity kill *PDE3A* high-expressing cancer cell lines. They all induced PDE3A–SLFN12 complex formation, as has been described for the compound DNMDP[18]. A structural understanding of the interaction of these diverse compounds with PDE3A will probably inform future optimization of PDE3A–SLFN12-directed cancer therapeutics. Our finding that vanadium-containing compounds selectively kill cancer cells expressing high levels of the sulfate transporter *SLC26A2* was also surprising, given that a mechanistic link between the two had not been previously suspected. A recent study showed that SLC26A2 expression is a mechanism of resistance to TNF-related apoptosis-inducing ligand-induced cell death[38]; it remains to be determined whether that mechanism is relevant to vanadium-induced killing and whether these compounds dysregulate sulfate homeostasis. Perhaps most interesting was our observation that the drug tepoxalin has the unique ability to inhibit cells that express high levels of the multidrug resistance gene *ABCB1*. While tepoxalin was originally developed as a cyclooxygenase/5-lipoxygenase inhibitor, our structure–activity relationship studies clearly showed that tepoxalin's anticancer activity is probably cyclooxygenase- and 5-lipoxygenase-independent. While we showed that ABCB1 is both necessary and sufficient to confer tepoxalin cytotoxicity, the precise mechanism by which such cell death occurs is to be established. Further optimization of tepoxalin against this new target, and engineering out the drug's cyclooxygenase/5-lipoxygenase inhibitory activity, would probably result in improved tolerability as an anticancer agent.

Historically, a challenge with cell-based phenotypic screens is the difficulty in gaining molecular insight into the mechanism of action of hit compounds. However, our results in the present study demonstrate the power of genome-scale CRISPR–Cas9 loss-of-function and gain-of-function screens to provide mechanistic clues to small-molecule action. For example, both CRISPR knockout and CRISPR activation screens pointed to ABCB1 as the most relevant target of tepoxalin. The availability of such functional genomic screening methods will probably reinvigorate cell-based screening more broadly. We also note that, whereas small molecules are typically thought of as inhibitors of their protein targets, our PRISM results indicate that this is often not the case. For example, we discovered compounds that stabilize protein–protein interaction (for example, PDE3A–SLFN12) and that engage ABCB1 but do not kill cells by ABCB1 inhibition. A plethora of noninhibitory small-molecule activities probably remains to be discovered from this PRISM dataset. However, we note that when anticancer drug targets are not themselves cancer dependencies, it is possible that strong selective pressure will result in downregulation of the target protein, resulting in drug resistance. Such drug resistance could presumably be overcome through combination drug treatment, as is the norm for most types of cancer.

The PRISM barcoding and pooling approach described in this study substantially increases screening efficiency, but it is conceivable that the pooling of cell lines results in paracrine-mediated mechanisms that modulate drug sensitivity. In practice, however, we have yet to observe such cell–cell interactions or any consistent discordance between PRISM and one-by-one viability profiling. Nevertheless, we and others have reported the existence of microenvironment-mediated drug resistance mechanisms[39]; the potential for such interactions should be considered when interpreting the PRISM results.

The PRISM Repurposing dataset described in this study represents nearly half of all drugs ever tested in humans. Given the large number of unexpected findings that emerged from this initial screen, we believe that expansion of the PRISM resource in both the dimension of drugs and cancer models is warranted. Such data will provide an important pharmacological component of the Cancer Dependency Map (https://depmap.org), which in turn will form a preclinical foundation for cancer precision medicine.

Methods

Cell lines. Parental cell lines were obtained from the Broad Institute-Novartis Institutes for BioMedical Research Cancer Cell Line Encyclopedia (CCLE) project[10] before PRISM barcoding (see https://portals.broadinstitute.org/ccle for the original sources). For the follow-up studies, LS1034, HeLa and HEK293T cells were purchased from the ATCC. The REC1, SF295, OVISE, COLO 320, HT-29 and SNU-449 cell lines were provided by CCLE. Wild-type and ABCB1-overexpressing (pLX_317 vector) Kuramochi cell lines were gifts from E. Stover[40]. HeLa PDE3A CRISPR knockout cells (PDE3A$^{-/-}$ cells) were described previously[18]. LS1034, SF295, COLO 320, SNU-449 and OVISE cell lines derived with Cas9 were provided by the Cancer Dependency Map (Broad Institute). Short tandem repeat (STR) fingerprinting was performed by Genetica using the PowerPlex 16 HS system (Promega Corporation). STR profiles were compared with STR profiles reported by vendors and in literature. Misidentified cell lines or other STR conflicts are listed in Supplementary Table 9. These cell lines are flagged in the data files and are not shown by default in the website interface. Cell lines were confirmed to be negative for *Mycoplasma* using the MycoScope PCR Mycoplasma Detection Kit (Genlantis). The LS1034, REC1, OVISE, SF295, COLO 320, SNU-449 and Kuramochi cell lines were cultured in Roswell Park Memorial Institute (RPMI) medium (Thermo Fisher Scientific). HeLa cells were cultured using DMEM (Thermo Fisher Scientific). All media were supplemented with 10% heat-inactivated FCS (Sigma-Aldrich) and 1% penicillin-streptomycin G (Thermo Fisher Scientific) except for the HEK293T cell line, which was maintained without antibiotics.

PRISM screening. We made several improvements to the PRISM barcoding method described previously[4]. The assay employs a 24-nucleotide barcode stably introduced into cancer cell lines via lentiviral transduction. The barcode is located at the end of the blasticidin resistance gene and is expressed as an mRNA under the highly active PGK promoter. We adapted the mRNA capture and Luminex detection method developed for the L1000 gene expression assay[41] to detect PRISM barcodes to improve throughput. In addition to using an mRNA-based readout, assay improvements included pooling cell lines according to doubling time similarity, collapsing lysate plates together before detection and adding a spike-in barcode control for amplification and detection.

The detailed PRISM assay protocol is available online at https://depmap.org/repurposing. Briefly, barcoded cell lines were pooled (25 cell lines per pool) based on doubling time and frozen into assay-ready vials. Vials were thawed and 1 pool was immediately plated per 384-well assay plate at 1,250 cells per well in triplicate. Cells were either treated the following morning with compounds by pin transfer (repurposing primary and secondary high-throughput screens) or plated directly onto assay-ready plates containing compounds (used for follow-up in the lower-scale MTS004 and MTS006 screens). After a 5-d incubation, cells were lysed. Lysate plates containing 1 pool of 25 cell lines each were then pooled together further to yield 1 (in the secondary screen) or 2 (in the primary screen) final detection pools for amplification and barcode measurement. For the secondary screen, a set of ten unique barcodes were spiked into each well before PCR to control for variation in PCR amplification and Luminex detection following lysate pooling.

Data processing. Luminex median fluorescence intensity (MFI) values were calculated as the median fluorescence values of all beads corresponding to a single PRISM barcode in a single technical replicate. MFI values were $\log_2$-transformed (logMFI) and subjected to two quality control steps. First, an 'outlier pool filter' was applied to remove probable screening artifacts (Extended Data Fig. 2). In each assay plate, logMFI values were median centered per cell line and each well was summarized by the median of these centered MFI values. Wells more than five median absolute deviations from the median across all wells from the same compound plate and plate location were removed. Second, a 'control separation filter' was applied. For each plate, cell lines with strictly standardized mean difference[42] values <2 were excluded from the rest of the analysis (Extended Data Fig. 3). Strictly standardized mean difference values were calculated as:

$$\frac{(\mu_{-}-\mu_{+})}{\sqrt{\sigma_{-}^{2}+\sigma_{+}^{2}}}$$

where $\mu_{-/+}$ and $\sigma_{-/+}$ stand for the medians and the median absolute deviations of the logMFI values computed over the negative/positive control wells for each cell line on each plate. The number of PRISM profile cell line replicates passing quality control is shown in Extended Data Fig. 4.

A total of 1,448 compounds were selected for secondary eight-point dose–response testing based on reproducibility, predictability, selectivity and compound availability (Supplementary Table 2). For the secondary screen only, ten unique barcodes were spiked into each well of each plate after cell lysis. Normalized MFI values were computed by taking the ratio of each logMFI value to the median logMFI of the inert barcodes in each well. For data produced before the spike-in protocol was introduced, normalized MFI values were set equal to MFI values.

Fold change values were calculated as the ratio of normalized MFI to the median of the normalized MFI from dimethylsulfoxide (DMSO)-treated negative controls for each cell line on each plate. The batch effects produced from variable detection and assay conditions were then removed using ComBat (located in the sva package; we used version 3.30.1 of sva)[43]. ComBat was run over each treatment condition separately by considering the $\log_2$-transformed fold change values as the probes and the pool-replicate combinations as the batches. The corrected log fold change values were then median collapsed for each cell line, screen, source plate and well combination. We labeled cell lines as sensitive to a treatment if the median-collapsed fold change was <0.3.

Dose–response analysis. Dose–response relationships were obtained by fitting four-parameter logistic curves to viability values for each compound and cell line using the R package drc (version 3.0-1). Following the practice of Smirnov et al.[44], the upper asymptote of the logistic curves was fixed at 1 and the viability values were fitted as a function of drug concentration according to:

$$V(c)=E_{\infty}+\frac{1-E_{\infty}}{1+\mathrm{e}^{\mathrm{HS}(c-\mathrm{EC}_{50})}}$$

where all concentrations are in the natural logarithm scale. IC_{50} values were defined as the concentration c at which $V(c)=0.5$. Additionally, the dose–response area under the curve (AUC) was calculated using the normalized integral:

$$\mathrm{AUC}=\frac{\int_{c_{\min}}^{c_{\max}}V(c)\mathrm{d}c}{c_{\max}-c_{\min}}$$

This formulation puts AUC values on a scale between 0 and 1 for curves with lower asymptotes <1, where lower AUC values indicate increased sensitivity to treatment.

Biomarker discovery. To generate predictive biomarkers, we adopted the ATLANTIS predictive models[9] and trained multiple models for each PRISM profile. ATLANTIS is a tailored nonlinear regression model for gene dependency prediction based on the baseline characteristics of cancer cell lines. More specifically, ATLANTIS is an efficient implementation of a conditional inference forest[45] with additional weighting and iterative feature selection steps. Implementation details have been published previously[9] and the code is available on a public repository (https://github.com/cancerdatasci/atlantis).

For each dose-wise log fold change profile, 14 ATLANTIS models are trained (1 model per feature set). Feature sets include baseline cell line omics, genetic dependencies and experimental confounders. All feature sets are listed in Supplementary Table 10.

Next, the predictive performance of each model was assessed based on the Pearson correlation between out-of-bag model predictions and the response variable. Models with Pearson correlations greater than 0.2 were strong models. The relative importance of each feature (mean decrease in accuracy) was computed by ATLANTIS for each model. The most important feature of each strong predictive model is presented as a potential predictive biomarker or strongly associated phenotype. The comprehensive list of biomarkers is available at https://depmap.org/repurposing.

Compound killing selectivity. To assess for selective killing activity, the bimodality coefficient[8] for each median-collapsed log fold change PRISM profile was computed for each compound as follows:

$$\frac{g^{2}+1}{k+3(n-1)^{2}/(n-2)(n-3)}$$

where n is the number of samples (cell lines), g is the sample skewness and k is the sample excess kurtosis. Note that a larger bimodality coefficient implies a highly skewed (large magnitude of g) but light-tailed (small kurtosis) distribution.

Computation of AUC values for cross-dataset comparison. Secondary PRISM Repurposing data were compared to CTD^2 (v.2.0, accessed 15 December 2015) and GDSC available through the PharmacoGX package (version 1.12.0)[17,44]. For the PRISM Repurposing and GDSC datasets, dose–response curves were fitted as described earlier. CTD^2 provides dose–response curve parameters and curves were not refitted. The scope of the comparison was limited to compounds screened in all three datasets with a minimum overlapping fourfold dose range across the datasets. Dose–response curves were computed for each compound-cell line dataset combination using all available doses. AUC values were calculated over the shared dose range (curves were not refitted). The complete table of the published/recomputed dose–response parameters and AUC values are given in Supplementary Table 11.

Assessment of noise in the PRISM Repurposing dataset. The s.e.m. of the inferred log fold change viability values was calculated to estimate the amount of noise in the PRISM screen. We assumed that (spike-in) normalized logMFI values have a cell line-specific additive noise with a constant variance σ^2 across treatments. An s.e.m. propagation analysis (see section 9.3 of Chatfield[46]), gives the following:

$$\sigma_{\text{log fold change}} = \sqrt{\frac{\sigma^2_{\text{treatment}} + \sigma^2_{\text{control}}}{n_{\text{rep}}}} \approx \sigma\sqrt{\frac{1 + 1/n_{\text{control}}}{n_{\text{rep}}}}$$

where n_{rep} is the number of replicates (3 for PRISM Repurposing), n_{control} is the number of negative control wells in a given plate (32 in the standard PRISM assay format) and $\sigma_{\text{log fold change}}$ is the s.e.m. estimate; σ was estimated separately for each cell line and plate using normalized, negative-control $\log_2$ MFI values. σ estimates for the same cell line were median-collapsed and used to calculate the $\sigma_{\text{log fold change}}$. This procedure was applied separately to each PRISM Repurposing screen. In MTS006, DMSO-only plates were used.

Projection of viability profiles to two dimensions. The log viability profiles from the primary screen were embedded into a two-dimensional manifold using the UMAP[7] algorithm and are visualized in Fig. 2a. Cell lines that were missing more than 10% of their viability values (failed in the quality-control steps) were removed and the remaining missing values were imputed using the R package FastImputation (version 2.0)[47]. UMAP was applied to the resulting data, using the cosine distance metric and the following configuration parameters: 7 nearest neighbors; 0.5 minimum distance; 2 components; and 200 training epochs. The rest of the parameters were set to the defaults provided by the R package umap (version 0.2.3.1). For the visualization, we filtered out compounds with an average Pearson replicate correlation below 0.25. Mechanisms of action that include fewer than 20 compounds are shown in translucent gray.

Comparison to genetic loss-of-function screens. Linear models were fitted to test the association between the primary collapsed log fold change profiles of each drug and the DepMap Avana CRISPR knockout gene effect scores using the lmFit function from the limma R package (version 3.38.3) with default parameters[48]. *P* values were corrected within each dose profile for multiple hypotheses using the Benjamini–Hochberg method. For primary data, a single profile was selected to test for each drug. The procedure was repeated for secondary collapsed log fold change profiles. A single dose series was selected for each drug.

Compounds for confirmatory studies. Paclitaxel (catalog no. S1150), tyrphostin AG-1296 (catalog no. S8024), anagrelide HCl (catalog no. S3172), levonorgestrel (catalog no. S1727), deoxycorticosterone acetate (catalog no. S4243), drospirenone (catalog no. S1377) and norethindrone (catalog no. S4040) were purchased from Selleck Chemicals. Dofequidar fumarate (catalog no. SML0938), N,N′-Bis(salicylidene)-o-phenylenediamine vanadium(IV) oxide complex (catalog no. 68541) and vanadium(IV) oxide sulfate hydrate (catalog no. 233706) were purchased from Sigma-Aldrich. Tepoxalin (catalog no. T103205) was purchased from Toronto Research Chemicals and WuXi AppTec (custom synthesis). DCEBIO (catalog no. 1422) and zardaverine (catalog no. 1046) were purchased from Tocris. Disulfiram (HY-B0240), bortezomib (HY-10227) and tanaproget (HY-15606) were purchased from MedChemExpress. BMOV (FB18735) was purchased from Carbosynth. Tetrathiomolybdate (catalog no. AC389530010) was purchased from Thermo Fisher Scientific. Danazol (catalog no. 1500220) was purchased from Microsource. Gestrinone (catalog no. Prestw-1267) was purchased from Prestwick.

Synthesis of RWJ20142. Reactions were monitored by thin-layer chromatography with 0.25 mm Merck precoated silica gel plates (60 F_{254}) and Waters Alliance HT LC/MS system (Waters 2998 UV/Visible Detector, Waters ACQUITY SQD mass spectrometer and Waters e2795 Sample Manager) using a Waters CORTECS C18 column (3 × 30 mm^2, 2.7 µm particle size). Additional parameters were: solvent gradient, 97% A at 0 min, 5% A at 1.75 min, 97% A at 2.28 min, total 2.60 min; solvent A, water (MILLIQ) + 0.01% formic acid (Sigma-Aldrich); solvent B, acetonitrile (EMD Millipore) + 0.01% formic acid; flow rate, 1.75 ml min^{-1}. Purification of reaction products was carried out by flash chromatography using CombiFlash Rf with Isco RediSep Rf High Performance Gold (Teledyne ISCO) or SiliaSep High Performance (SiliCycle) columns (4, 12, 24, 40, 80 or 120 g). ^{1}H nuclear magnetic resonance and ^{13}C nuclear magnetic resonance spectra were obtained using a 400 Ascend (Bruker). Chemical shifts are reported relative to chloroform ($\delta = 7.24$) for ^{1}H nuclear magnetic resonance.

In a 100 ml oven-dried flask, a solution of lithium hexamethyldisilazide (10 ml, 10 mmol, 1.0 M in tetrahydrofuran (THF)) was added dropwise to a solution of 1-(4-chlorophenyl)ethanone (1.10 g, 7.14 mmol) in dry THF (20 ml) at −78 °C under argon atmosphere. After 1 h, a solution of dihydrofuran-2,5-dione (0.86 g, 8.52 mmol) in dry THF (10 ml) was added at −78 °C, stirred for 30 min and then warmed up to room temperature. After 2 h, the reacting mixture was quenched with water, acidified with 1 N HCl (pH 2), then extracted with dichloromethane (3 × 10 ml^2). The combined organic layers were dried over Na_2SO_4, filtered and concentrated. The residue was purified by column chromatography on silica gel (10–50% ethanol ethylacetate in hexanes) to afford 6-(4-chlorophenyl)-4,6-dioxohexanoic acid (550 mg, 31% yield). LC–MS: MS (ESINeg) $m/z = 253$ [M-H]$^-$.

In a 50 ml flask, a solution of (4-methoxyphenyl)hydrazine hydrochloride (0.37 g, 2.12 mmol), 6-(4-chlorophenyl)-4,6-dioxohexanoic acid (0.49 g, 1.93 mmol) and triethylamine (0.31 ml, 2.31 mmol) in methanol (30 ml) was stirred overnight at room temperature. The reaction was quenched with 5% HCl aqueous solution (pH 2), then extracted with dichloromethane (3 × 10 ml^2). The combined organic layers were dried over Na_2SO_4, filtered and concentrated. The residue was purified by column chromatography on silica gel (20–60% ethanol ethylacetate in hexanes) to afford 3-[5-(4-chlorophenyl)-1-(4-methoxyphenyl)pyrazol-3-yl]propanoic acid (285 mg, 42% yield). LC–MS: MS (ESINeg) $m/z = 355$ [M-H]$^-$. ^{1}H nuclear magnetic resonance (400 MHz, chloroform-D) $\delta = 10.25$ (brs, 1 H), 7.27 (d, $J = 8.5$ Hz, 2 H), 7.20–7.12 (m, 4 H), 6.87 (d, $J = 8.9$ Hz, 2 H), 6.35 (s, 1 H), 3.82 (s, 3H), 3.07 (t, $J = 7.5$ Hz, 2 H), 2.83 (t, $J = 7.5$ Hz, 2H). Compound purity >97% was quantified by LC–MS.

Synthesis of BEOV. Vanadyl sulfate trihydrate (25 g, 115 mmol) dissolved in 25 ml of water was added to ethyl maltol (43.4 g, 310 mmol) dissolved in 125 ml of hot water under argon; the resulting solution was heated gently with stirring for 30 min. The pH was adjusted very slowly to 8.5 by adding NaOH (12.7 g, 319 mmol) in 10 ml of water. The resulting mixture was refluxed for 2 h and then allowed to cool to room temperature. The dark blue–gray solid was collected by vacuum filtration, washed with cold water and dried in a vacuum to produce BEOV with a yield of 88%. The compound was 93% pure by LC–MS.

Cloning. The pXPR_003 and pXPR_023 vectors were acquired from the Genetic Perturbation Platform (GPP; Broad Institute). The oligonucleotides for sgRNA design were generated using Broad GPP sgRNA guide generator resource (https://portals.broadinstitute.org/gpp/public/analysis-tools/sgrna-design) and the respective oligonucleotides were synthesized by Integrated DNA Technologies. To clone the sgRNAs into either the pXPR_003 guide-only or pXPR_023 all-in-one CRISPR lentiviral expression systems, we followed the protocol available on the GPP website (https://portals.broadinstitute.org/gpp/public/resources/protocols). The CRISPR sgRNA sequences are shown in Supplementary Table 12.

Antibodies and western blot. The following antibodies were used: polyclonal rabbit anti-PDE3A (1:1,000; catalog no. A302-740A; Bethyl Laboratories); monoclonal mouse anti-V5 (1:5,000; catalog no. R960-25; Thermo Fisher Scientific); monoclonal rabbit anti-MDR1/ABCB1 (clone D3H1Q) (1:1,000; catalog no. 12683; Cell Signaling Technology); monoclonal mouse anti-β-actin (clone 8H10D10) (1:1,000; catalog no. 3700; Cell Signaling Technology); and monoclonal mouse anti-SLC26A2 (clone 3F6) (1:1,000 dilution; catalog no. H00001836-M04; Novus Biologicals). Cells were lysed with radioimmunoprecipitation assay buffer (CHAPS buffer substituted for Extended Data Fig. 8a) supplemented by protease and phosphatase inhibitors (Sigma-Aldrich). For the ABCB1 blots, proteins were transferred onto a nitrocellulose membrane using a Mini Trans-Blot Electrophoretic Transfer Cell (Bio-Rad Laboratories) in Tris-glycine buffer (Bio-Rad Laboratories) with 10% methanol for 4 h at 60 V and 4 °C. Membranes were blocked in Odyssey Blocking Buffer (LI-COR) for 1 h and probed overnight with primary antibodies. The following day, membranes were washed and probed with IRDye secondary antibodies (catalog nos. 926-68020 and 926-32211, each at a 1:5,000 dilution; LI-COR). For the PDE3A and V5 blots, different secondary antibodies were used (926-32210 and 926-68020, each at a 1:10,000 dilution; LI-COR). Blot images were collected with the Odyssey CLx imager (LI-COR).

Genomic DNA (gDNA) PCR and next-generation sequencing to quantify CRISPR editing frequency. To confirm efficient CRISPR cutting at the target loci, PCR primers were designed flanking the sgRNA cut site by 75–100 base pairs (bp) on either side. The human gDNA PCR primer sequences corresponding to the regions targeted by MDR1, SLC26A2 and MTF1 sgRNAs are shown in Supplementary Table 13. gDNA was isolated from knockout cell lines using the Gentra Puregene Kit (QIAGEN) and amplified with the primers to yield an amplicon roughly 150–250 bp in length using Herculase II Fusion Polymerase (Agilent Technologies). The PCR protocol involved a 2-min denaturation at 95 °C, followed by 24 cycles of 95 °C for 2 min, 55 °C for 2 min and 72 °C for 1 min. PCR samples were purified and submitted for the next-generation CRISPR sequencing assay at the Massachusetts General Hospital DNA Core. Knockout efficiency was assessed by the percentage of reads containing a frameshift caused by an indel compared to the total read count. Results for each guide were averaged across primer sets with successful amplification.

Cellular viability assays. Cells were seeded at a density of 2,000 cells per well (1,000 cells per well for the HeLa cell line) in a 96-well clear bottom black microplate (Corning). The following day, compounds were dispensed using the D300e Digital Dispenser (Tecan). Following incubation, viability was assessed by CellTiter-Glo (Promega Corporation). Luminescence was measured using an EnVision plate reader (PerkinElmer; EnVision Manager 1.13.3009.1401).

Independent replicate wells were averaged and normalized to vehicle control. Dose curves were generated using Prism 8 (GraphPad Software).

PDE3A coimmunoprecipitation assay. The PDE3A immunoprecipitation and western blotting of coprecipitated SLFN12-V5 protein experiments were performed as described previously[18]. Briefly, HeLa cells were plated onto 15 cm plates at 3×10^6 cells per plate and transfected the next day with 15 µg of pLX307-SLFN12 plasmid (clone TRCN0000476272) using FuGENE 6 (Promega Corporation) at a 4:1 ratio. Roughly 72 h posttransfection, cells were treated with 10 µM of the repurposing hit compounds or 1 µM of DNMDP or 1 µM anagrelide for 6 h. Cells were collected and lysed with a modified radioimmunoprecipitation assay buffer (150 mM NaCl, 10% glycerol, 50 mM Tris-Cl pH 8.0, 50 mM $MgCl_2$, 1% NP-40 detergent), supplemented protease and phosphatase inhibitors. Immunoprecipitation was performed using 2 mg of total protein lysates and 1 µg of anti-PDE3A antibody at 4 °C overnight, followed by incubation with 7.5 µl each of Protein A and Protein G Dynabeads (10001D and 10003D; Thermo Fisher Scientific) at 4 °C for 1 h. Beads were washed with lysis buffer and proteins were eluted with 30 µl of lithium dodecyl sulfate–polyacrylamide gel electrophoresis loading buffer.

PDE3A and PDE3B enzyme activity assays. A commercial fluorescence polarization assay was performed using recombinant PDE3A and PDE3B by BPS Bioscience. Compounds were tested in duplicate at 9 concentrations in a half-logarithmic dilution series (top concentration of 10 µM) with a final DMSO concentration of 1%. The enzymatic reactions were conducted at room temperature for 60 min in a 50 µl mixture containing phosphodiesterase assay buffer, 100 nM FAM-cAMP, a PDE enzyme and the test compound. After the enzymatic reaction, 100 µl of a binding solution (1:100 dilution of the binding agent with the binding agent diluent) was added to each mix and the reaction was performed at room temperature for 15 min. Fluorescence intensity was measured at an excitation of 485 nm and an emission of 528 nm using an Infinite M1000 microplate reader (Tecan). Fluorescence intensity was converted to fluorescence polarization using the Magellan v.6 software (Tecan).

Differential scanning fluorimetry (thermal shift) analysis of compounds binding to PDE3A. The gene for PDE3A (residues 677–1,141) was codon-optimized for *Escherichia coli* expression (GeneArt; Thermo Fisher Scientific) and cloned into an expression vector that attached an N-terminal polyhistidine sequence followed by a Tobacco Etch Virus protease cleavage site. The protein was expressed in *E. coli* and purified by affinity and size-exclusion chromatography. The polyhistidine sequence was removed by the Tobacco Etch Virus protease. PDE3A (5 µM) was incubated for 20 min at room temperature with 100 µM of each compound. The reaction buffer was 20 mM HEPES, pH 7.4, 150 mM NaCl, 500 µM TCEP, 5 mM $MgCl_2$ and 1% DMSO. After incubation, SYPRO orange (Thermo Fisher Scientific) was added to give a final concentration of 10× relative to stock concentrate. Protein was tested using the LightCycler 480 (Roche Life Science). The temperature was increased from 25 to 95 °C using a gradient of $0.06\,°C\,s^{-1}$.

LS1034 CRISPR–Cas9 genome-wide knockout screen. The Brunello genome-scale sgRNA library was obtained from the Broad Institute GPP[49]. Virus was titrated to a goal infection efficiency of 0.3–0.6. LS1034-Cas9 cells were infected with Brunello virus in 12-well plates via centrifugation at 2,000 r.p.m. and 30 °C. The following day, cells were split into two replicate flasks and selected with $6\,\mu g\,ml^{-1}$ puromycin for 7 d. After selection, replicates were seeded into 16 µM tepoxalin (Wuxi) or DMSO control. Cells were maintained at 37 °C and 5% CO_2 in CellSTACK 1,272 cm^2 2-STACK flasks (Corning) in RPMI with 10% FCS. Cells were reseeded every 7 d at a minimum of 40 million cells per passage (to maintain approximately 500× library representation). Media and drugs were refreshed every 3–4 d for a total of 3 weeks. gDNA was isolated from cell pellets using the NucleoSpin Blood XL columns (MACHEREY-NAGEL). gDNA PCR and sequencing were performed by the Broad Institute GPP.

LS1034 CRISPR–dCas9 genome-wide activation screen. LS1034 cells were stably transduced with pXPR_109 to express dCas9-VP64 (ref. [50]). Selective induction of CD45 and CD4 expression using control guides was confirmed by flow cytometry. The Calabrese B genome-scale virus library was obtained from the Broad Institute GPP. LS1034-dCas9-VP64 cells were infected via centrifugation as described earlier. The following day, cells were split into two replicates and reseeded. The next day, $6\,\mu g\,ml^{-1}$ of puromycin was added. After selection for 6 d, replicates were split into DMSO or 16 µM tepoxalin (Wuxi) drug arms in duplicate and cultured for 2 weeks as described earlier. gDNA was isolated and sequenced as described earlier.

CRISPR screen analysis. Guides targeting multiple genes or with <50 reads in the plasmid DNA pool were filtered. Counts were normalized against total library size. The guide-level $\log_2$ fold change was computed using the ratio between treatment versus vehicle control counts. The results from all guides targeting each gene were averaged. Statistical significance for each gene-level result was calculated using the MAGeCK-MLE method, using the suggested number of permutation rounds (10; ref. [51]). Two-sided P values were corrected for multiple hypothesis testing using the Benjamini–Hochberg method.

Tepoxalin competition assay. LS1034-Cas9-firefly luciferase cells were cocultured in a 1:1 ratio with LS1034-*Renilla* luciferase cells, both infected with *ABCB1* sgRNA or a cutting control sgRNA. Cells were treated with 16 µM tepoxalin (Wuxi) or vehicle. The coculture was passaged every 4 d and reseeded with drug. Luciferase activity was quantified using the Dual-Glo Luciferase Assay System (Promega Corporation) and measured using an EnVision plate reader. Data points were collected at day 0 and every 4 d until 12 d of treatment. The firefly to *Renilla* luminescence ratio was normalized to the initial day 0 measurement.

Tepoxalin cell permeability and stability assays. Compounds were incubated in medium alone or with 1 million $cells\,ml^{-1}$ at 37 °C with gentle shaking for 3 h. Following incubation, cell samples were centrifuged at 500g for 5 min and washed twice with cold PBS. Cells were resuspended in 130 µl of water. Samples were sonicated and centrifuged at 3,000g for 15 min at 20 °C; 5 µl of supernatant was combined with 45 µl of cell media, 50 µl of water and 50 µl of acetonitrile containing internal standard. Samples were centrifuged again and a final 100 µl aliquot was transferred to a 96-well plate for analysis. Samples were analyzed on an ultra-performance liquid chromatography–tandem mass spectrometry system consisting of an ACQUITY UPLC I-Class FTN (Waters) and Triple Quad 4500 System (SCIEX) with compounds detected by positive mode multiple reaction monitoring detection. Mobile phase A consisted of water with 0.1% formic acid (catalog no. 33015-1L; Honeywell), while mobile phase B consisted of acetonitrile with 0.1% formic acid. The gradient ran from 10 to 95% B over 0.8 min at a flow rate of $0.9\,ml\,min^{-1}$. An ACQUITY BEH C18 1.7 m, $2.1 \times 50\,mm^2$ column (Waters) was used with column temperature maintained at 65 °C. Sample concentrations were determined using a standard curve and dilution quality-control samples prepared in a surrogate matrix. The Analyst v.1.6.2 software was used for integration and calculation determination. For the stability study, 1 µM of tepoxalin was added to PBS, RPMI with 10% FCS or acetonitrile in duplicate and measured by mass spectrometry with time points prepared at 0, 24, 48 and 72 h. The mass spectrometer was run in positive mode using multiple reaction monitoring detection for tepoxalin and the internal standard (75 nM midazolam).

Tepoxalin drug synergy/antagonism assays. Tepoxalin or paclitaxel were added in a dose–response matrix to LS1034 or REC1 cells, and viability was assessed by CellTiter-Glo. For the drug combination viability data, we first normalized CellTiter-Glo measurements by the median over DMSO wells on each plate. We then used the R package synergyfinder (version 1.8.0)[52] to estimate Bliss synergy scores across all dose combinations, applying synergyfinder's default baseline correction method. Synergy values for each drug combination and cell line were summarized by the synergy score with the highest magnitude across dose combinations (maximum synergy). We verified that similar results were obtained qualitatively using other synergy models (for example, Loewe, highest single agent and zero interaction potency) and methods for aggregating synergy scores across dose combinations (for example, averaging).

ABCB1 activity assays. The ABCB1 antagonism assay was performed by Eurofins using published methods[53]. Briefly, MDR1-MDCK cells were incubated with test compounds and calcein acetoxymethyl. Change in calcein acetoxymethyl concentration was assessed by fluorescence measurement. A second assay, MDR1-MDCK cell permeability, was performed by Cyprotex. Briefly, loperamide, a known MDR1 substrate, was added to the apical side of a cell monolayer and transport to the basal side was quantified over 60 min. Inhibition of MDR1-mediated transport of loperamide was assessed by adding tepoxalin or positive control (verapamil).

Transcriptional profiling by RNA-seq. LS1034 cells were seeded in 12-well plates. The following day, cells were treated in triplicate with 12 µM tepoxalin or DMSO vehicle control for 6 h. Wild-type SF295 cells and SF295 cells containing Cas9 and sgRNAs targeting GFP or MTF1 were plated in triplicate on a 6-well plate and incubated overnight. RNA was isolated using the RNeasy Mini Kit (QIAGEN) with DNase treatment. RNA quality was confirmed by Bioanalyzer (Agilent Technologies). Library preparation was performed by the Molecular Biology Core Facility at the Dana-Farber Cancer Institute using the KAPA mRNA HyperPrep Kit (Roche). Nucleic acid was sequenced using an Illumina NextSeq 500 PE75 instrument. Gene-level expression values were obtained from RNA-seq using the TOPMed RNA-seq pipeline (version 1)[54]. RSEM (version 1.3.0) was used to generate transcripts per million gene-level expression quantifications. These tools were run using the FireCloud and Terra platforms[55]. Differential gene expression was calculated using the DESeq2 package (version 1.22.2)[56].

Statistics and reproducibility. No statistical method was used to determine sample sizes. Compounds were plated for screening without regard to compound identity, but experiments were not randomized. No data were excluded from the analysis, except individual data points flagged as assay failures by the process described earlier. Statistical tests are described in the text and figure legends with their associated sample sizes. PRISM data were generated without the investigators' knowledge of compound and cell line identities during screening. Investigators were not blind to compound and cell line identities during the analysis. Further information on research design is available in the Nature Research Reporting Summary linked to this article.

Reporting Summary. Further information on research design is available in the Nature Research Reporting Summary linked to this article.

Data availability

The PRISM Repurposing dataset, including screening data and all metadata, is available at the Cancer Dependency Map portal (https://depmap.org/repurposing). Raw and processed PRISM viability data are available from the Cancer Dependency Map portal (https://depmap.org/repurposing) and have been archived via figshare (https://doi.org/10.6084/m9.figshare.9393293). Interactive versions of Figs. 2a and 4 (with accompanying raw data) are also available on the Cancer Dependency Map portal; scatter plot source data are also deposited in figshare. The cell line features used for biomarker analysis are listed in Supplementary Table 10 and archived via figshare (https://doi.org/10.6084/m9.figshare.10277810). RNA-seq data have been deposited with the Gene Expression Omnibus (accession number GSE133299). All other data supporting the findings of this study are available from the corresponding author upon reasonable request.

Code availability

Data analysis was performed in R v.3.5.1 using custom-made or publicly available R packages. Individual packages are explicitly cited in the manuscript. The custom code is available upon request and from GitHub (https://github.com/broadinstitute/repurposing).

Received: 15 October 2019; Accepted: 6 December 2019;
Published online: 20 January 2020

References

1. Alley, M. C. et al. Feasibility of drug screening with panels of human tumor cell lines using a microculture tetrazolium assay. *Cancer Res.* **48**, 589–601 (1988).
2. Garnett, M. J. et al. Systematic identification of genomic markers of drug sensitivity in cancer cells. *Nature* **483**, 570–575 (2012).
3. Basu, A. et al. An interactive resource to identify cancer genetic and lineage dependencies targeted by small molecules. *Cell* **154**, 1151–1161 (2013).
4. Yu, C. et al. High-throughput identification of genotype-specific cancer vulnerabilities in mixtures of barcoded tumor cell lines. *Nat. Biotechnol.* **34**, 419–423 (2016).
5. Corsello, S. M. et al. The Drug Repurposing Hub: a next-generation drug library and information resource. *Nat. Med.* **23**, 405–408 (2017).
6. Ben-David, U. et al. Genetic and transcriptional evolution alters cancer cell line drug response. *Nature* **560**, 325–330 (2018).
7. McInnes, L., Healy, J., Saul, N. & Großberger, L. UMAP: Uniform manifold approximation and projection. *J. Open Source Softw.* **3**, 861 (2018).
8. Ellison, A. M. Effect of seed dimorphism on the density-dependent dynamics of experimental populations of *Atriplex triangularis* (Chenopodiaceae). *Am. J. Bot.* **74**, 1280–1288 (1987).
9. Tsherniak, A. et al. Defining a cancer dependency map. *Cell* **170**, 564–576.e16 (2017).
10. Barretina, J. et al. The cancer cell line encyclopedia enables predictive modelling of anticancer drug sensitivity. *Nature* **483**, 603–607 (2012).
11. Ghandi, M. et al. Next-generation characterization of the Cancer Cell Line Encyclopedia. *Nature* **569**, 503–508 (2019).
12. Li, H. et al. The landscape of cancer cell line metabolism. *Nat. Med.* **25**, 850–860 (2019).
13. Meyers, R. M. et al. Computational correction of copy number effect improves specificity of CRISPR–Cas9 essentiality screens in cancer cells. *Nat. Genet.* **49**, 1779–1784 (2017).
14. McFarland, J. M. et al. Improved estimation of cancer dependencies from large-scale RNAi screens using model-based normalization and data integration. *Nat. Commun.* **9**, 4610 (2018).
15. Aben, N., Vis, D. J., Michaut, M. & Wessels, L. F. A. TANDEM: a two-stage approach to maximize interpretability of drug response models based on multiple molecular data types. *Bioinformatics* **32**, i413–i420 (2016).
16. Rydenfelt, M., Wongchenko, M., Klinger, B., Yan, Y. & Blüthgen, N. The cancer cell proteome and transcriptome predicts sensitivity to targeted and cytotoxic drugs. *Life Sci. Alliance* **2**, e201900445 (2019).
17. Iorio, F. et al. A landscape of pharmacogenomic interactions in cancer. *Cell* **166**, 740–754 (2016).
18. de Waal, L. et al. Identification of cancer-cytotoxic modulators of PDE3A by predictive chemogenomics. *Nat. Chem. Biol.* **12**, 102–108 (2016).
19. Karin, M. et al. Human metallothionein genes are clustered on chromosome 16. *Proc. Natl Acad. Sci. USA* **81**, 5494–5498 (1984).
20. Skrott, Z. et al. Alcohol-abuse drug disulfiram targets cancer via p97 segregase adaptor NPL4. *Nature* **552**, 194–199 (2017).
21. Nechushtan, H. et al. A phase IIb trial assessing the addition of disulfiram to chemotherapy for the treatment of metastatic non-small cell lung cancer. *Oncologist* **20**, 366–367 (2015).
22. Eckschlager, T., Adam, V., Hrabeta, J., Figova, K. & Kizek, R. Metallothioneins and cancer. *Curr. Protein Pept. Sci.* **10**, 360–375 (2009).
23. Irth, H., de Jong, G. J., Brinkman, U. A. & Frei, R. W. Metallic copper-containing post-column reactor for the detection of thiram and disulfiram in liquid chromatography. *J. Chromatogr.* **370**, 439–447 (1986).
24. Tsvetkov, P. et al. Mitochondrial metabolism promotes adaptation to proteotoxic stress. *Nat. Chem. Biol.* **15**, 681–689 (2019).
25. Iljin, K. et al. High-throughput cell-based screening of 4910 known drugs and drug-like small molecules identifies disulfiram as an inhibitor of prostate cancer cell growth. *Clin. Cancer Res.* **15**, 6070–6078 (2009).
26. Taylor, A. M. et al. Genomic and functional approaches to understanding cancer aneuploidy. *Cancer Cell* **33**, 676–689.e3 (2018).
27. Koboldt, D. C. et al. Comprehensive molecular portraits of human breast tumours. *Nature* **490**, 61–70 (2012).
28. Bell, D. Integrated genomic analyses of ovarian carcinoma. *Nature* **474**, 609–615 (2011).
29. Wang, J., Yuen, V. G. & McNeill, J. H. Effect of vanadium on insulin sensitivity and appetite. *Metabolism* **50**, 667–673 (2001).
30. Thompson, K. H. et al. Vanadium treatment of type 2 diabetes: a view to the future. *J. Inorg. Biochem.* **103**, 554–558 (2009).
31. Hästbacka, J. et al. The diastrophic dysplasia gene encodes a novel sulfate transporter: positional cloning by fine-structure linkage disequilibrium mapping. *Cell* **78**, 1073–1087 (1994).
32. Hästbacka, J. et al. Identification of the Finnish founder mutation for diastrophic dysplasia (DTD). *Eur. J. Hum. Genet.* **7**, 664–670 (1999).
33. *Analysis-Ready Standardized TCGA Data from Broad GDAC Firehose 2016_01_28 Run* (Broad Institute TCGA Genome Data Analysis Center, 2016); https://doi.org/10.7908/C11G0KM9
34. Argentieri, D. C. et al. Tepoxalin: a dual cyclooxygenase/5-lipoxygenase inhibitor of arachidonic acid metabolism with potent anti-inflammatory activity and a favorable gastrointestinal profile. *J. Pharmacol. Exp. Ther.* **271**, 1399–1408 (1994).
35. *Animal Drugs at FDA: Tepoxalin* (Food and Drug Administration, accessed 15 December 2019); https://animaldrugsatfda.fda.gov/adafda/views/#/home/previewsearch/141-193
36. Dubey, R. et al. Chromatin-remodeling complex SWI/SNF controls multidrug resistance by transcriptionally regulating the drug efflux pump ABCB1. *Cancer Res.* **76**, 5810–5821 (2016).
37. Waldman, S. A. et al. Pharmacokinetics and pharmacodynamics of tepoxalin after single oral dose administration to healthy volunteers. *J. Clin. Pharmacol.* **36**, 462–468 (1996).
38. Dimberg, L. Y. et al. A genome-wide loss-of-function screen identifies SLC26A2 as a novel mediator of TRAIL resistance. *Mol. Cancer Res.* **15**, 382–394 (2017).
39. Straussman, R. et al. Tumour micro-environment elicits innate resistance to RAF inhibitors through HGF secretion. *Nature* **487**, 500–504 (2012).
40. Stover, E. H. et al. Pooled genomic screens identify anti-apoptotic genes as targetable mediators of chemotherapy resistance in ovarian cancer. *Mol. Cancer Res.* **17**, 2281–2293 (2019).
41. Subramanian, A. et al. A next generation connectivity map: L1000 platform and the first 1,000,000 profiles. *Cell* **171**, 1437–1452.e17 (2017).
42. Zhang, X. D. A pair of new statistical parameters for quality control in RNA interference high-throughput screening assays. *Genomics* **89**, 552–561 (2007).
43. Johnson, W. E., Li, C. & Rabinovic, A. Adjusting batch effects in microarray expression data using empirical Bayes methods. *Biostatistics* **8**, 118–127 (2007).
44. Smirnov, P. et al. PharmacoGx: an R package for analysis of large pharmacogenomic datasets. *Bioinformatics* **32**, 1244–1246 (2016).
45. Strobl, C., Boulesteix, A.-L., Kneib, T., Augustin, T. & Zeileis, A. Conditional variable importance for random forests. *BMC Bioinformatics* **9**, 307 (2008).
46. Chatfield, C. *Statistics for Technology: a Course in Applied Statistics* 3rd edn (CRC Press, 2018).
47. Honaker, J., King, G. & Blackwell, M. Amelia II: a program for missing data. *J. Stat. Softw.* https://www.jstatsoft.org/article/view/v045i07 (2011).
48. Ritchie, M. E. et al. limma powers differential expression analyses for RNA-sequencing and microarray studies. *Nucleic Acids Res.* **43**, e47 (2015).
49. Doench, J. G. et al. Optimized sgRNA design to maximize activity and minimize off-target effects of CRISPR-Cas9. *Nat. Biotechnol.* **34**, 184–191 (2016).
50. Sanson, K. R. et al. Optimized libraries for CRISPR-Cas9 genetic screens with multiple modalities. *Nat. Commun.* **9**, 5416 (2018).
51. Li, W. et al. Quality control, modeling, and visualization of CRISPR screens with MAGeCK-VISPR. *Genome Biol.* **16**, 281 (2015).
52. He, L. et al. in *Cancer Systems Biology: Methods and Protocols* (ed von Stechow, L.) 351–398 (Springer, 2018).
53. Polli, J. W. et al. Rational use of in vitro P-glycoprotein assays in drug discovery. *J. Pharmacol. Exp. Ther.* **299**, 620–628 (2001).

54. Aguet, F. et al. Genetic effects on gene expression across human tissues. *Nature* **550**, 204–213 (2017).
55. Birger, C. et al. FireCloud, a scalable cloud-based platform for collaborative genome analysis: strategies for reducing and controlling costs. Preprint at *bioRxiv* https://doi.org/10.1101/209494 (2017).
56. Love, M. I., Huber, W. & Anders, S. Moderated estimation of fold change and dispersion for RNA-seq data with DESeq2. *Genome Biol.* **15**, 550 (2014).

Acknowledgements

We thank C. Yu, W. Hahn, B. Wolpin, A. Bass, N. Gray, K. Stegmaier, E. Stover, T. Lewis, M. Mesleh, A. Burgin, S. Alper, G. Botta, M. Macaluso, P. Tsvetkov, X. Jin, K. Blakeslee, G. Ciolek and E. Lander for helpful scientific discussions. M. Passino, C. Zhu, K. Gore, M. Laird, C. Trapechio and E. Parikh generated the barcoded PRISM cell lines and performed the assays. K. Stumbraite assisted with STR fingerprinting. S. Johnson and J. Davis performed lysate processing and detection. S.E. Johnston and R. Singh provided analytical chemistry support. A. Vrcic, C. Sandland and S. Figueroa-Lazu assisted with compound management. G. Kugener and A. Gonzalez provided technical assistance. This study was supported in part by the Carlos Slim Foundation (Slim Initiative in Genomic Medicine for the Americas), the Next Generation Fund at the Broad Institute of MIT and Harvard (S.M.C.), the Conquer Cancer Foundation of ASCO Young Investigator Award (S.M.C.) and National Institutes of Health grants nos. U01 HG008699 (T.R.G and A.S.), U54 HL127366 (T.R.G and A.S.), KL2 TR002542 (S.M.C.) and K08 CA230220 (S.M.C.).

Author contributions

S.M.C., M.K., J.G.B., J.A.B., J.S.B., C.C.M., A.T. and T.R.G. conceptualized the study. S.M.C., R.T.N., R.D.S., M.K., J.G.B., D.P., E.L., R.N., J.A.B., C.C.M., A.T. and T.R.G. devised the study methodology. J.R., M.K., J.G.B., V.M.W., E.L., R.N., P.M., Y.C., M.G.R. and L.W. operated the software. S.M.C., R.T.N., R.D.S., J.R., M.K. and J.G.B. validated the data. S.M.C., J.R., M.K., J.G.B., V.M.W., J.M.M. and L.W. carried out the formal analysis. S.M.C., R.T.N., R.D.S., J.R., M.K., J.G.B., R.H., D.P., X.W., S.A.B., C.W.G., N.J.L., U.B.-D., N.D., P.J.O., C.N.H., A.S. and C.C.M. carried out the investigation. E.S., J.G.D., H.G., M.M., F.V., A.S., J.A.R., J.A.B., A.T. and T.R.G. managed the resources. S.M.C., R.D.S. and S.A.B. curated the data. S.M.C., R.T.N., R.D.S., J.R., M.K., J.G.B., R.H., X.W., V.M.W., A.A.T., S.A.B., U.B.-D., J.M.M., A.T., and T.R.G. wrote the original draft. M.G.R. and N.D. reviewed and edited the draft. J.R., M.K., V.M.W., A.A.T., P.M. and B.T.W. oversaw data visualization. M.M., A.T. and T.R.G. supervised the study. S.A.B., A.S., J.A.R. and C.C.M. oversaw the project administration. S.M.C., J.S.B. and T.R.G. acquired the funding.

Competing interests

S.M.C., X.W., H.G., M.M., A.S. and T.R.G. receive research funding unrelated to this project from Bayer HealthCare. M.M. receives research funding from Ono and serves as a scientific advisory board and consultant for OrigiMed. M.M. has patents licensed to LabCorp and Bayer. M.M. and T.R.G. were formerly consultants and equity holders in Foundation Medicine, which was acquired by Roche. J.A.B. is an employee and shareholder of Vertex Pharmaceuticals. J.G.D. and A.T. consult for Tango Therapeutics. T.R.G. is a consultant to GlaxoSmithKline and is a founder of Sherlock Biosciences. Patent applications for the drug uses detailed in this manuscript have been filed. The other authors declare no competing interests.

Additional information

Extended data is available for this paper at https://doi.org/10.1038/s43018-019-0018-6.

Supplementary information is available for this paper at https://doi.org/10.1038/s43018-019-0018-6.

Correspondence and requests for materials should be addressed to T.R.G.

Reprints and permissions information is available at www.nature.com/reprints.

Publisher's note Springer Nature remains neutral with regard to jurisdictional claims in published maps and institutional affiliations.

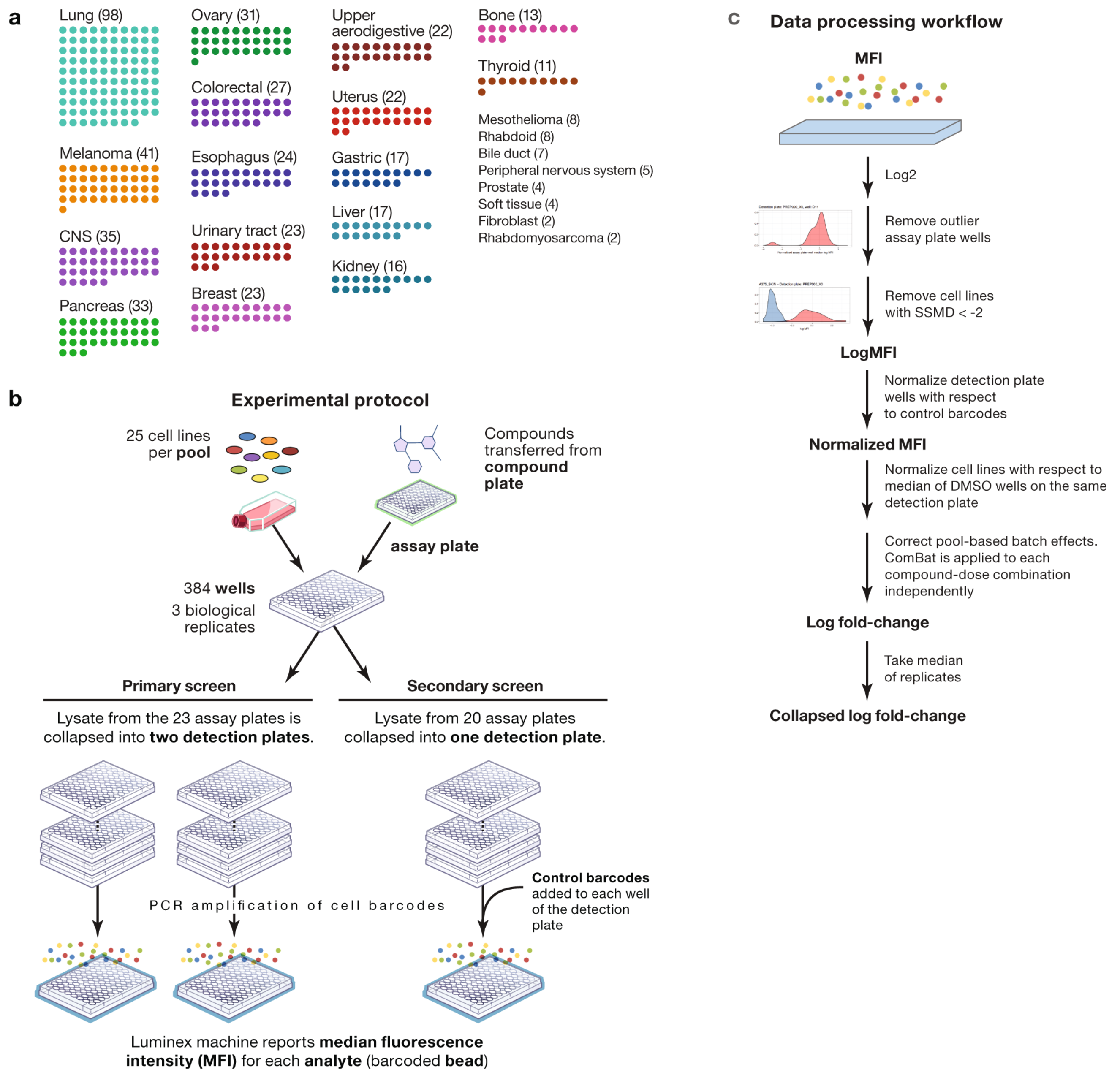

Extended Data Fig. 1 | PRISM Repurposing assay and data processing overview. a, Lineage diversity of PRISM cell lines. The 489+ cancer cell lines tested span more than 23 tumor types. Lineages with fewer than 10 cell lines are listed on the right. **b**, Experimental protocol. Cell lines are grouped by doubling time into pools of approximately 25 cell lines. One pool is plated onto each assay plate. Compounds are transferred by pin transfer from a source compound plate (HTS and HTS002 screens), or cells are plated directly onto assay-ready plates generated by acoustic dispensing of compounds (MTS004, MTS005, and MTS006 screens). In either case, compound plates are shared by all replicates of each treatment condition. After incubation and lysis, all assay plates generated by a given compound plate are grouped and collapsed into 3 (HTS002, MTS005, and MTS006 screens) or 6 (HTS, MTS004 screens) detection plates so that each detection plate receives 1 or zero copies of each pool. Ten control barcodes are then spiked into each detection plate well (HTS002, MTS005, and MTS006 screens). Detection plates are amplified by PCR and detected using Luminex FLEXMAP 3D instruments. **c**, Data processing workflow. Median Fluorescence Intensity (MFI) values are calculated from fluorescence values for each replicate-condition-cell line combination and are log2-transformed. Assay plates wells are normalized, median-collapsed, and compared to the normalized medians of other assay plate wells in the same well position that have been dosed by the same compound plate. A robust z-score is calculated, and assay plate wells with a |z-score| > 5 are filtered. Strictly standardized mean differences (SSMD) are calculated between positive and negative control conditions for each cell line on each assay plate. Cell line-assay plate combinations with SSMD < 2 are filtered by a control-separation filter to generate the log MFI data matrix. In datasets with control barcodes added, data are normalized with respect to the median of control barcodes to generate the MFI normalized data matrix. Data are DMSO-normalized and pooling artifacts are corrected using ComBat to generate the log fold change data matrix. Up to 3 independently treated plates (range 1-3 based QC filtering) in one screen are median-collapsed to generate the collapsed log fold change data matrix.

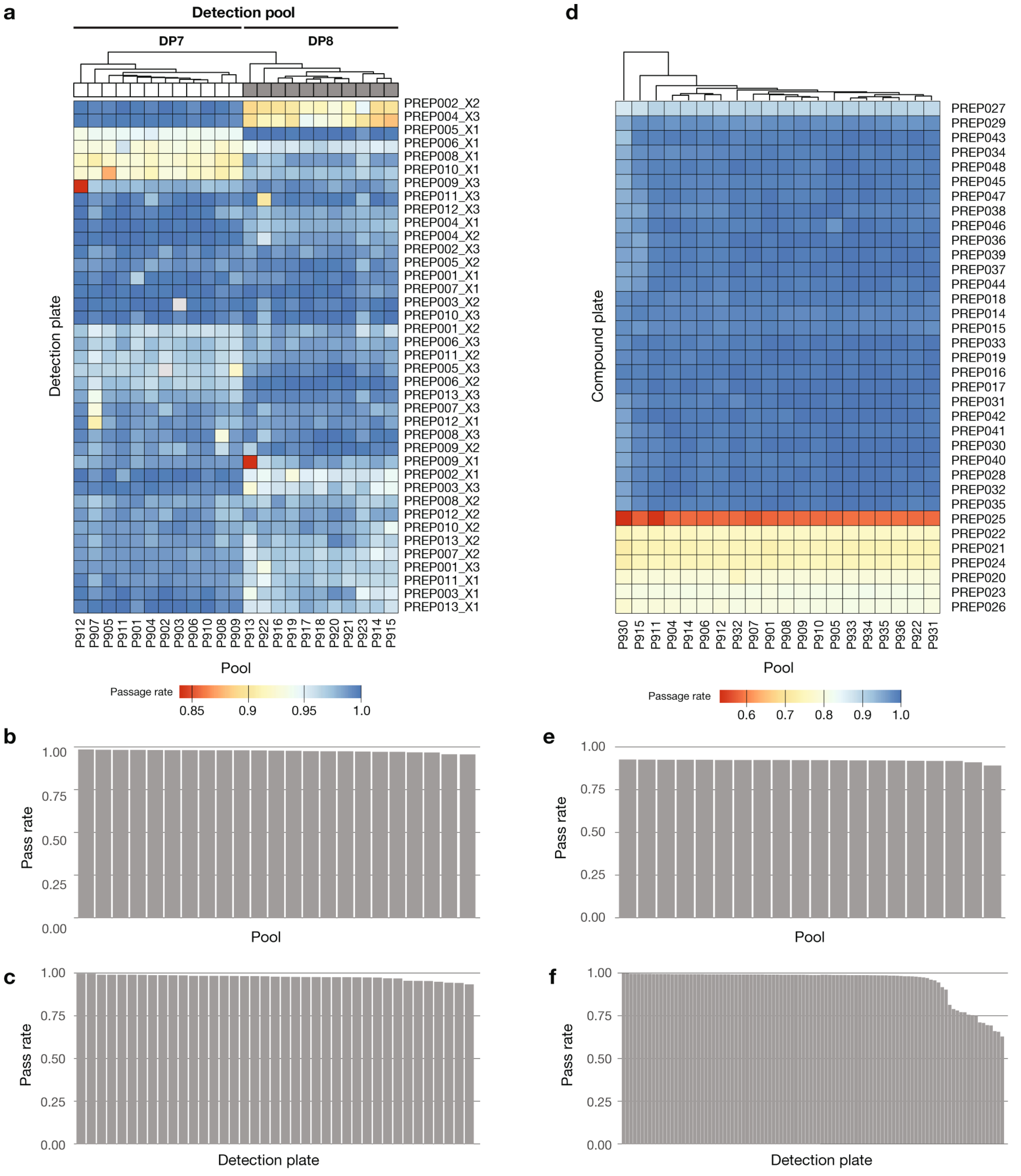

Extended Data Fig. 2 | Outlier pool QC filter to detect pool-level failures. a, Primary screen QC pass rate by pool. The fraction of treated assay plate-wells that pass the outlier filter is indicated. Cell line log MFI data are median-centered, and the medians of assay plate-wells are compared within each well-detection plate combination. Extreme outliers with |robust z-score| >5 are filtered. **b**, Primary screen QC pass rate by detection plate. **c**, Primary screen QC pass rate of assay plates. Overall pass rate was high (median 98.6%, minimum 83.8%). **d**, Secondary screen QC pass rate by pool. **e**, Secondary screen QC pass rate by detection plate. The pass rate is above 95% for 81% of detection plates. **f**, Secondary screen QC pass rate by plate-pool combinations. 3 replicate plates are combined for visualization. Overall pass rate was high (median 99.1%, mean 94.3%), where failures are almost exclusively coming from 7 detection plates, implying failure at final detection step. Across the screen, 5.7% of the pools are filtered out as outliers.

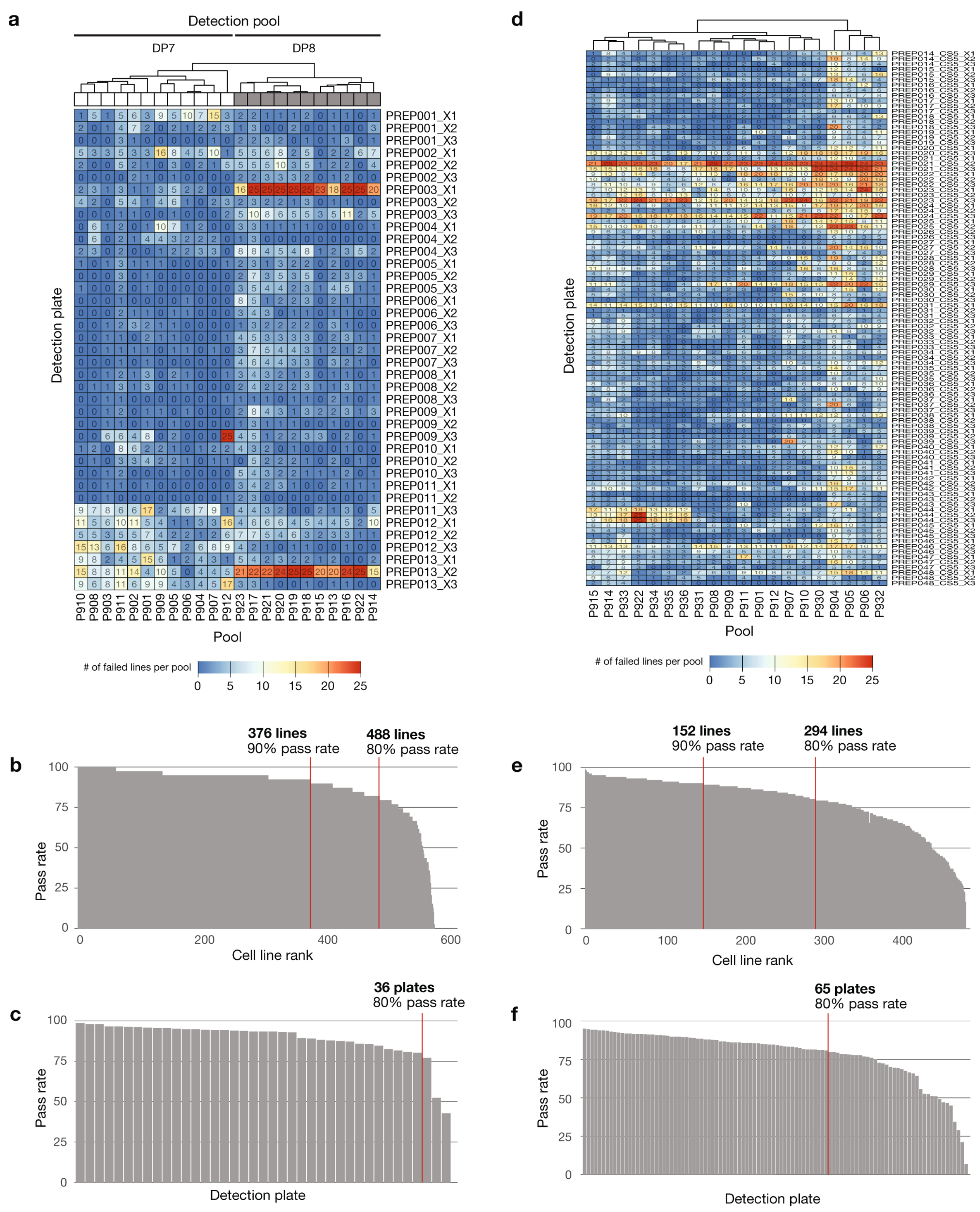

	P910	P908	P903	P911	P902	P901	P909	P905	P906	P904	P907	P912	P923	P917	P921	P920	P919	P918	P915	P913	P916	P922	P914
PREP001_X1	1	5	1	5	6	3	9	5	10	7	15	3	2	2	1	1	1	2	0	1	1	0	1
PREP001_X2	2	0	1	4	7	2	0	2	1	2	2	3	1	3	0	0	2	0	0	1	0	0	3
PREP001_X3	0	0	0	3	1	0	0	0	0	0	1	0	2	2	3	2	0	1	0	1	3	0	1
PREP002_X1	5	3	3	5	3	3	16	8	4	5	10	1	5	5	6	8	2	5	0	2	2	6	7
PREP002_X2	2	0	0	5	2	1	0	3	0	2	1	5	5	5	5	10	3	5	1	2	2	0	4
PREP002_X3	0	0	0	0	2	1	0	1	0	0	0	0	2	2	3	3	3	2	0	1	2	0	0
PREP003_X1	2	3	1	3	1	1	3	5	2	2	0	0	16	25	25	25	25	25	23	18	25	25	20
PREP003_X2	4	2	0	5	4	1	4	6	1	0	2	3	2	3	2	2	1	3	0	1	1	0	0
PREP003_X3	0	0	0	1	1	0	0	1	0	0	0	2	5	10	8	6	5	5	3	5	11	2	5
PREP004_X1	0	6	1	2	0	1	10	7	1	2	0	0	3	3	1	1	1	1	0	0	0	0	1
PREP004_X2	0	6	0	2	1	4	4	3	2	2	2	0	1	3	0	0	0	0	0	0	0	0	0
PREP004_X3	2	3	0	2	0	0	1	2	2	3	3	0	8	8	4	5	4	8	1	2	3	5	2
PREP005_X1	1	0	1	3	1	1	1	0	0	0	0	1	2	3	1	3	2	2	0	2	0	0	0
PREP005_X2	0	0	0	3	0	1	0	0	0	0	0	0	2	7	3	5	3	5	0	2	3	3	1
PREP005_X3	1	0	0	2	0	1	0	0	0	0	0	0	3	5	4	4	2	3	1	4	5	1	1
PREP006_X1	0	0	0	1	0	0	0	0	1	0	0	0	8	5	1	2	2	3	0	2	1	1	1
PREP006_X2	0	0	0	2	1	1	0	1	1	0	0	0	3	4	3	0	1	1	0	1	1	0	0
PREP006_X3	0	0	1	2	3	2	1	1	0	0	0	0	1	3	2	2	2	2	0	3	1	0	0
PREP007_X1	0	0	1	1	0	2	1	1	0	0	0	1	4	5	3	3	3	3	0	2	3	1	1
PREP007_X2	0	0	1	1	1	1	0	1	1	0	1	0	3	7	5	4	4	3	1	2	1	2	1
PREP007_X3	0	0	0	1	0	1	0	0	0	0	0	0	4	6	4	4	3	3	0	3	2	1	0
PREP008_X1	0	0	1	2	1	3	0	2	1	0	0	1	3	4	3	2	1	3	0	1	1	0	1
PREP008_X2	0	1	1	3	1	3	0	1	1	0	0	0	2	4	2	2	2	3	1	1	3	1	1
PREP008_X3	0	0	1	1	0	0	0	0	0	0	0	1	1	1	1	0	1	1	0	2	1	0	1
PREP009_X1	0	0	1	2	0	1	1	0	1	0	0	0	2	8	4	3	1	3	2	2	3	1	3
PREP009_X2	0	0	1	1	0	1	0	1	0	0	0	0	1	3	1	1	1	0	0	1	0	0	0
PREP009_X3	0	0	6	6	4	8	0	2	0	0	0	25	4	5	1	2	2	3	3	0	2	0	1
PREP010_X1	1	2	0	8	6	2	2	1	0	1	2	2	4	3	2	0	1	0	0	0	1	0	0
PREP010_X2	0	1	0	3	3	4	2	2	1	0	1	1	0	5	2	2	2	1	0	2	0	1	0
PREP010_X3	0	0	1	2	0	0	0	1	0	0	0	0	5	4	3	2	2	1	1	1	2	0	1
PREP011_X1	0	0	1	1	0	1	0	0	0	0	0	0	3	4	2	3	1	0	0	2	1	1	1
PREP011_X2	0	0	1	0	0	0	0	0	0	0	0	1	2	3	0	0	0	0	0	0	0	0	1
PREP011_X3	9	7	8	6	6	17	2	4	6	7	9	1	4	4	3	2	0	0	2	1	3	0	5
PREP012_X1	11	5	6	10	11	5	4	1	1	3	3	16	4	6	6	6	4	5	4	4	5	2	10
PREP012_X2	5	5	3	5	5	7	4	2	2	1	2	6	7	7	5	4	6	3	2	3	3	1	1
PREP012_X3	15	13	6	16	8	6	5	7	2	6	8	9	4	2	1	0	1	1	0	0	1	0	0
PREP013_X1	9	8	2	4	5	15	6	1	2	4	3	1	5	4	2	3	2	2	1	2	0	0	2
PREP013_X2	15	8	8	11	14	4	10	5	0	4	4	5	21	22	22	24	25	25	20	20	24	25	15
PREP013_X3	9	6	8	11	6	9	9	4	3	4	5	17	3	3	1	0	0	1	0	1	1	0	0

Extended Data Fig. 3 | Control-separation QC filter to detect cell line failures. aa, Primary screen QC pass rate by cell line. SSMD of log MFI values is calculated between positive control and negative control treatments for each cell line on each plate. Data from cell line-plates with SSMD < 2 are filtered. **b**, Primary screen QC pass rate by detection plate. **c**, Primary screen QC pass rate of assay plates. Overall pass rate was high (median 99.2%, mean 94.3%). Some detection plates show higher failure rates for specific detection pools, implying failure at final detection step. The bulk of the filtered data was from two detection plate-detection pools (PREP013_X2 and PREP003_X1 in detection pool 8). **d**, Secondary screen QC pass rate by cell line. SSMD of log MFI values is calculated between positive control and negative control treatments for each cell line on each assay plate. Data from cell line-plates with SSMD < 2 are filtered. **e**, Secondary screen QC pass rate by detection plate. **f**, Secondary screen QC pass rate of assay plates. Overall pass rate was lower than primary (median 99.88%, mean 79.1%). Similar to the primary screen, the main mode of failure is platewise failures.

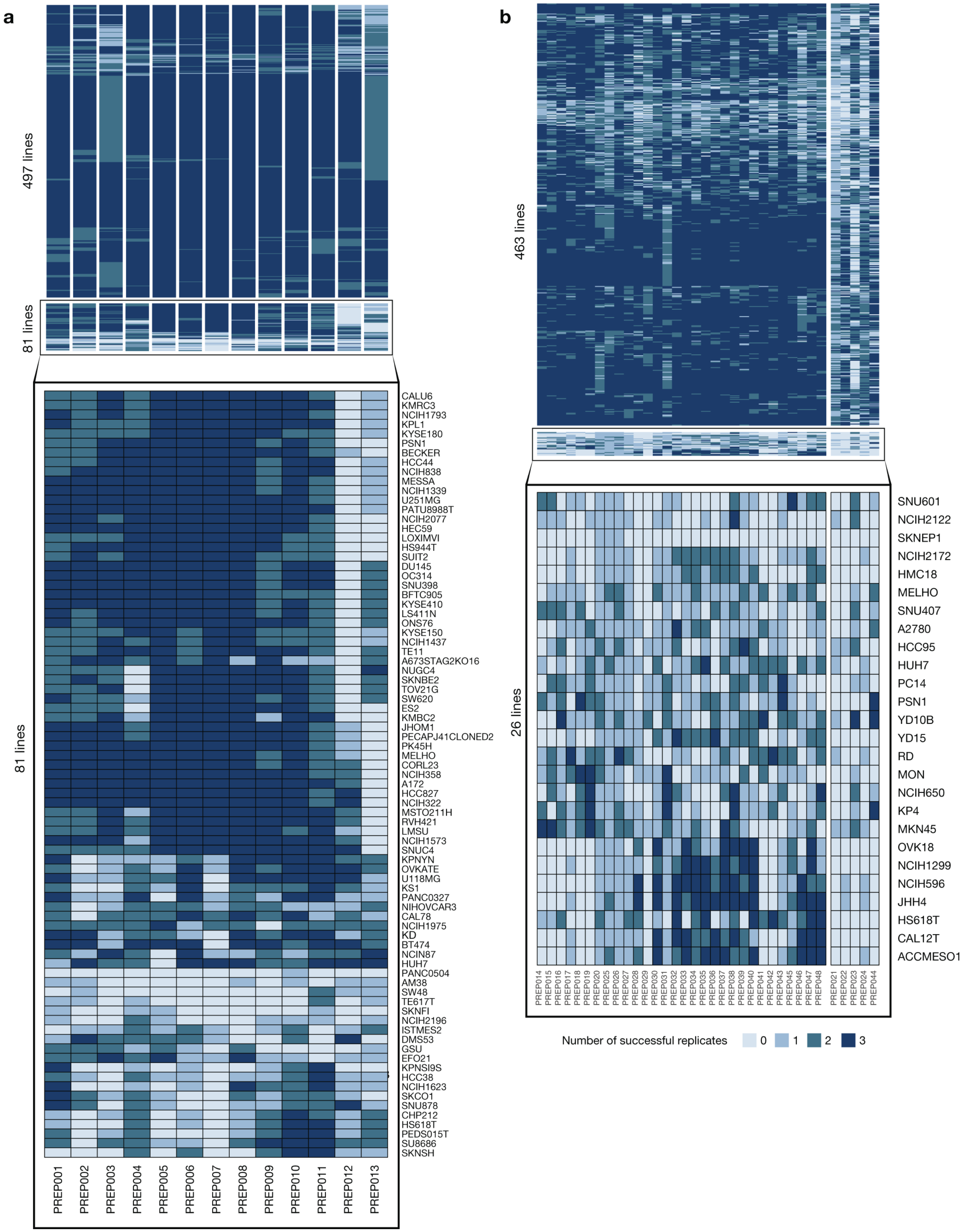

Extended Data Fig. 4 | Number of well replicates passing QC in the PRISM screens. a, Number of individual cell assay well replicates (max n = 3) that pass QC filters in the primary screen, grouped by compound plate and cell line quality. 86% (497 out of 578) of the cell lines have at least one passing replicate for all compound plates. Identity of cell lines with lower quality data are listed at the bottom. **b**, Number of individual cell assay well replicates (max n = 3) that pass QC filters in the secondary screen. 95% (463 out of 489) of cell lines have at least 1 passing replicate on at least 85% (30 out of 35) of the compound plates.

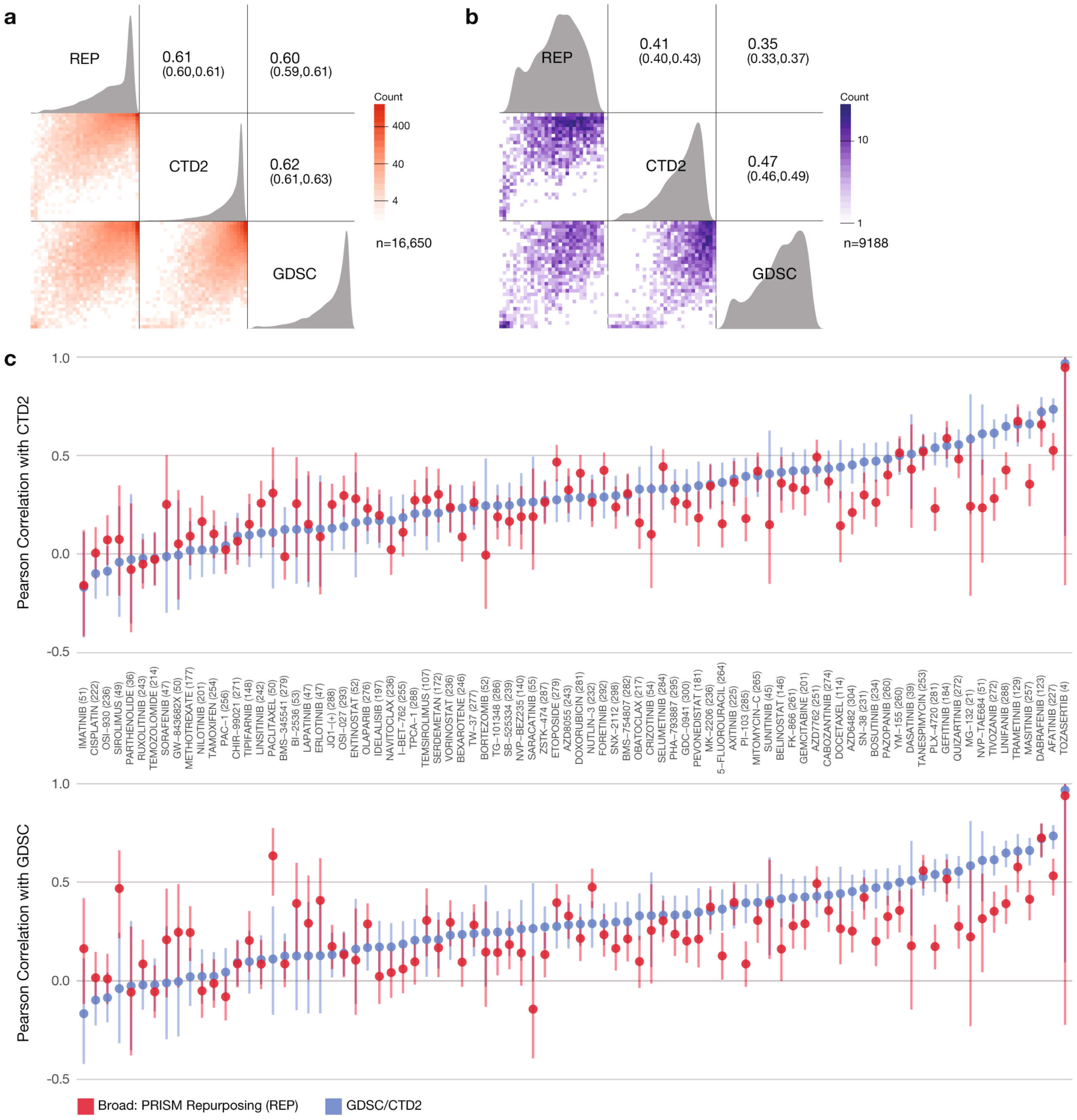

Extended Data Fig. 5 | Comparison of PRISM viability data to reference datasets. **a**, Pairwise Pearson correlations between drug response AUCs of publicly available datasets. AUC values were recomputed for 84 compounds and 318 cell lines (median 236 cell lines per compound) over the same dose-range for each compound-cell line pair in all 3 datasets (GDSC, CTD2, REP), and capped at 1. The Pearson correlation across shared compound-cell line pairs of the datasets is above 0.6. 44.8% of cell line-compound pairs show inactivity ($AUC > 0.8$) in all three datasets ($n = 16650$ compound-cell line pairs). **b**, Pairwise Pearson correlations between drug response AUCs after removing inactive cell line-compound pairs. Pearson correlations were re-calculated after filtering out the inactive data points ($AUC > 0.8$ in at all three datasets) ($n = 9188$ compound-cell line pairs). **c**, Compound-wise correlation between publicly available datasets. Correlation between PRISM data and other datasets is similar to correlation between other datasets. Points represent Pearson correlations and error bars represent 95% confidence intervals computed using Fisher's z-transform. GDSC vs. CTD2 is in blue and REP vs. GDSC/CTD2 is in red. The number of cell lines shared by all three datasets is shown after each drug name. Paired t-tests on compound-wise correlations show statistically significant (two-sided p-value: 0.012 and 0.014 for top and bottom, respectively) but small mean of differences (0.049 and 0.039 for top and bottom, respectively). The number of data points used to compute each correlation is given in the figure for each compound.

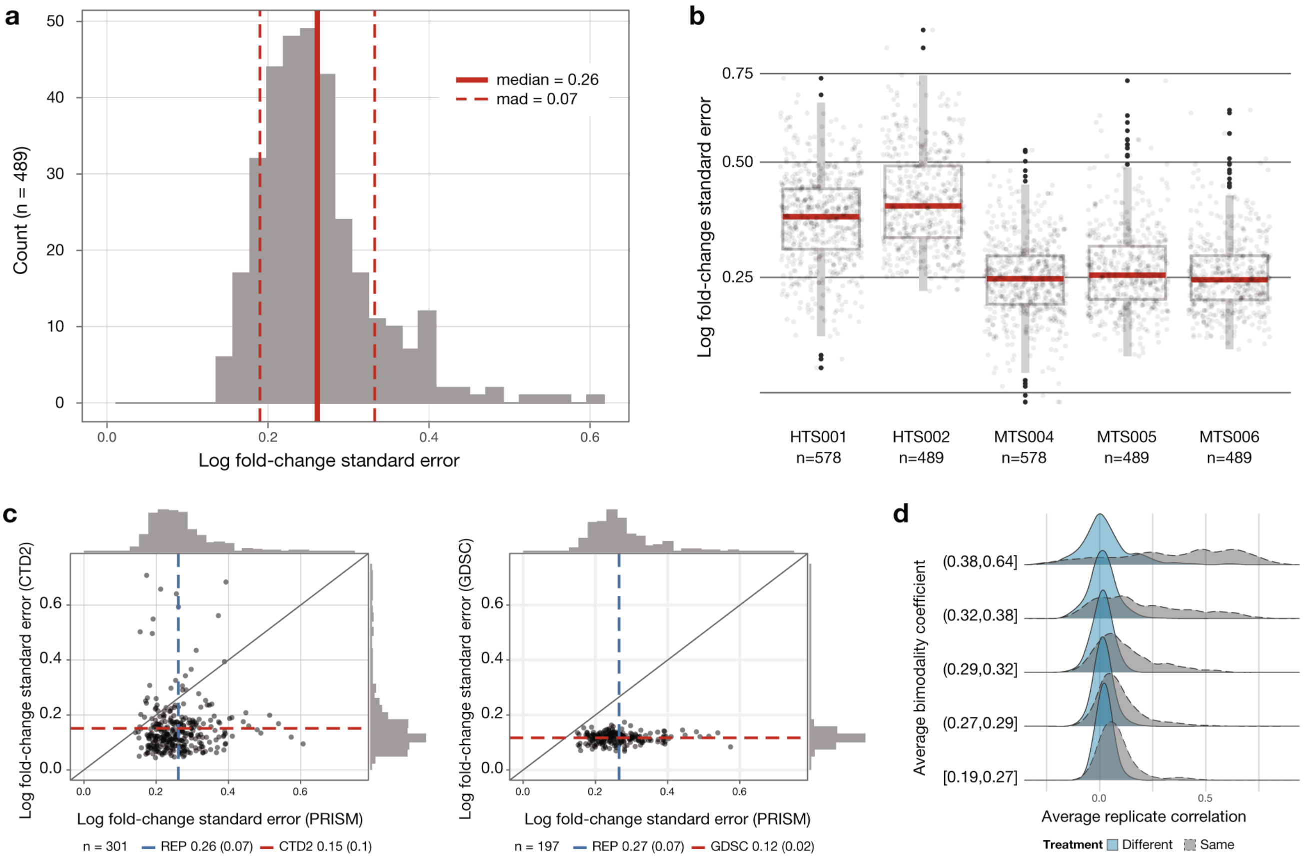

Extended Data Fig. 6 | PRISM Repurposing noise quantification. **a**, Cell line standard error estimates across vehicle-treated wells on PRISM plates treated with DMSO (n = 489 cell lines). Log fold change standard errors are estimated for each cell line using DMSO-only plates included in the MTS006 screen (n = 384 × 3 replicate wells for each cell line). **b**, Comparison of standard error estimates across screens. The error estimate calculation is repeated for each screen using DMSO wells on standard compound plates (n = 32 replicate wells per plate), except for MTS006, which uses DMSO-only plates (n = 384 replicate wells per plate). Higher noise levels are observed in the initial high-throughput screens HTS001 (n = 578 cell lines) and HTS002 (n = 489 cell lines) compared with the medium-throughput screens MTS004 (n = 578 cell lines), MTS005 (n = 489 cell lines), and MTS006 (n = 489 cell lines). Upper box limits, center lines, and lower box limits correspond to 75th, 50th, and 25th percentiles, respectively. Whiskers extend from the box limits to the most extreme value up to 1.5 IQR from the median. All cell lines are depicted as points, regardless of outlier status. **c**, Comparison of estimated standard error of vehicle control wells between high-throughput pharmacogenomic datasets. The average standard error across cell lines (n = 301 cell lines for PRISM versus CTD2 and n = 197 for PRISM versus GDSC) is indicated by dashed lines with standard deviation in parentheses. **d**, Relationship between drug selectivity and replicate reproducibility in PRISM. Average Pearson correlation between replicates for each compound, dose, and screen combination is stratified by mean bimodality coefficient. For comparison, the null distribution for randomly paired compounds is shown in blue.

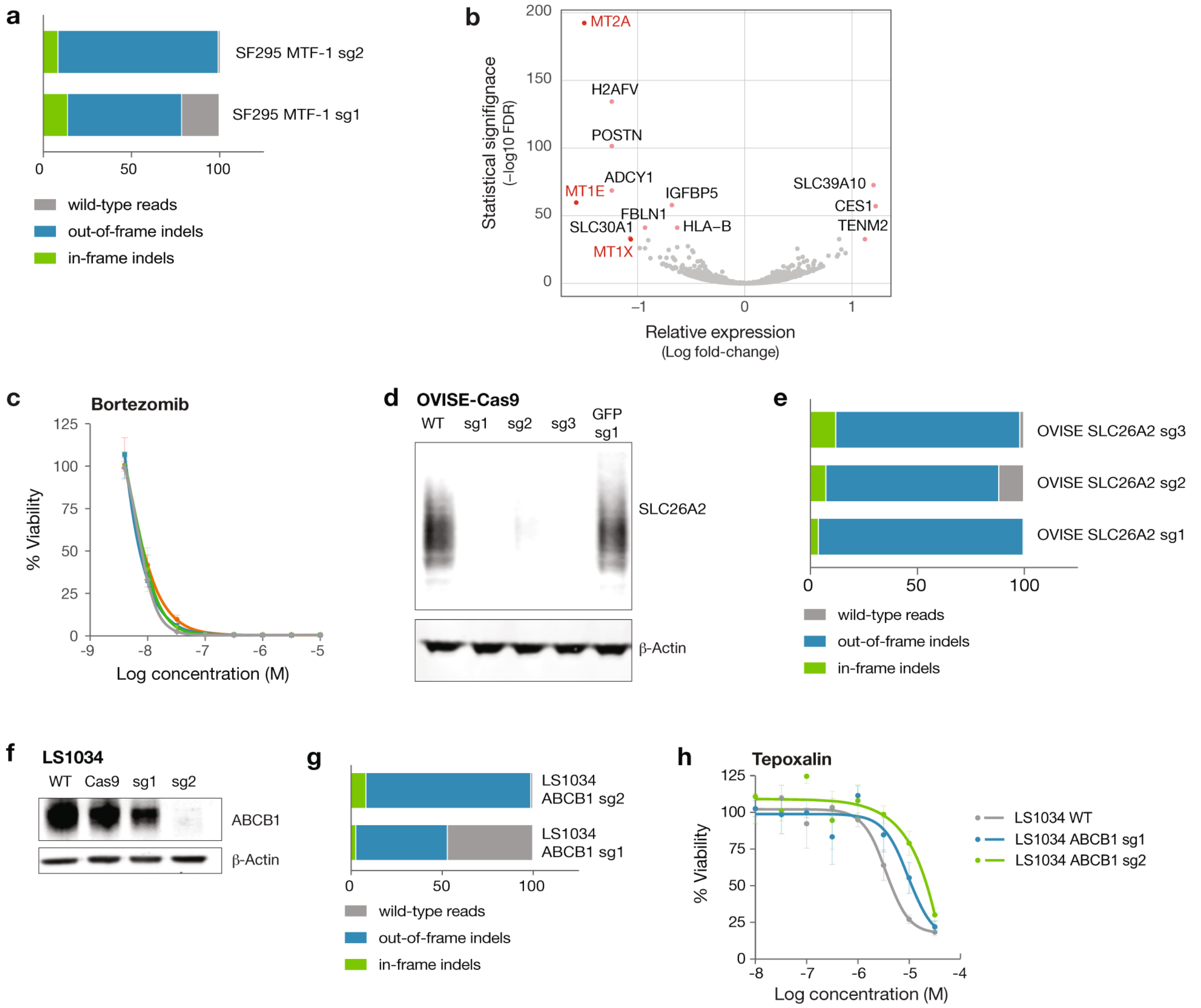

Extended Data Fig. 7 | Generation of knockout cell lines by CRISPR/Cas9 editing. a, SF295 cells were transduced with multiple guides targeting the MTF-1 gene. Following selection, genomic DNA was isolated, and the targeted region was amplified by PCR. Results from the NGS CRISPR assay are shown as percent indel formation. **b**, Differentially expressed genes in SF295 glioma cells following MTF-1 knockout by CRISPR/Cas9. Loss of MT1E, MT1X, and MT2A expression was observed upon MTF-1 knockout. Gene expression across three independent cell wells per cell line were measured by mRNA sequencing. Two-sided p-values for differential gene expression following MTF-1 knockout vs. parental cell line were calculated with DESeq2 and corrected for multiple hypothesis testing using the Benjamini-Hochberg method. **c**, Drug sensitivity of SF295 cells with and without MTF-1 knockout. MTF-1 does not alter sensitivity to control chemotherapeutic bortezomib. Mean viability across 3 independently treated wells is shown, with standard deviation indicated by error bars. **d**, Western immunoblot validation of SLC26A2 knockout in OVISE ovarian and A2058 melanoma cancer cell lines. The SLC26A2 protein is known to migrate across a range of molecular weights due to glycosylation. Results are representative of two independent experiments. **e**, OVISE cells were transduced with multiple guides targeting the SLC26A2 gene. Indel frequency at the SLC26A2 CRISPR Cas9 cut sites was assessed by NGS CRISPR assay. **f**, ABCB1 western blot with and without CRISPR knockout of ABCB1 in the LS1034 colon cancer cell line. Western blot was performed once. **g**, Percent indel formation at genomic cut site in LS1034 ABCB1 CRISPR knockout lines assessed by NGS CRISPR assay. **h**, Cellular viability of LS1034 CRISPR knockout lines after treatment with tepoxalin for 5 days. Mean viability across 3 independently treated wells is shown, with standard deviation indicated by error bars.

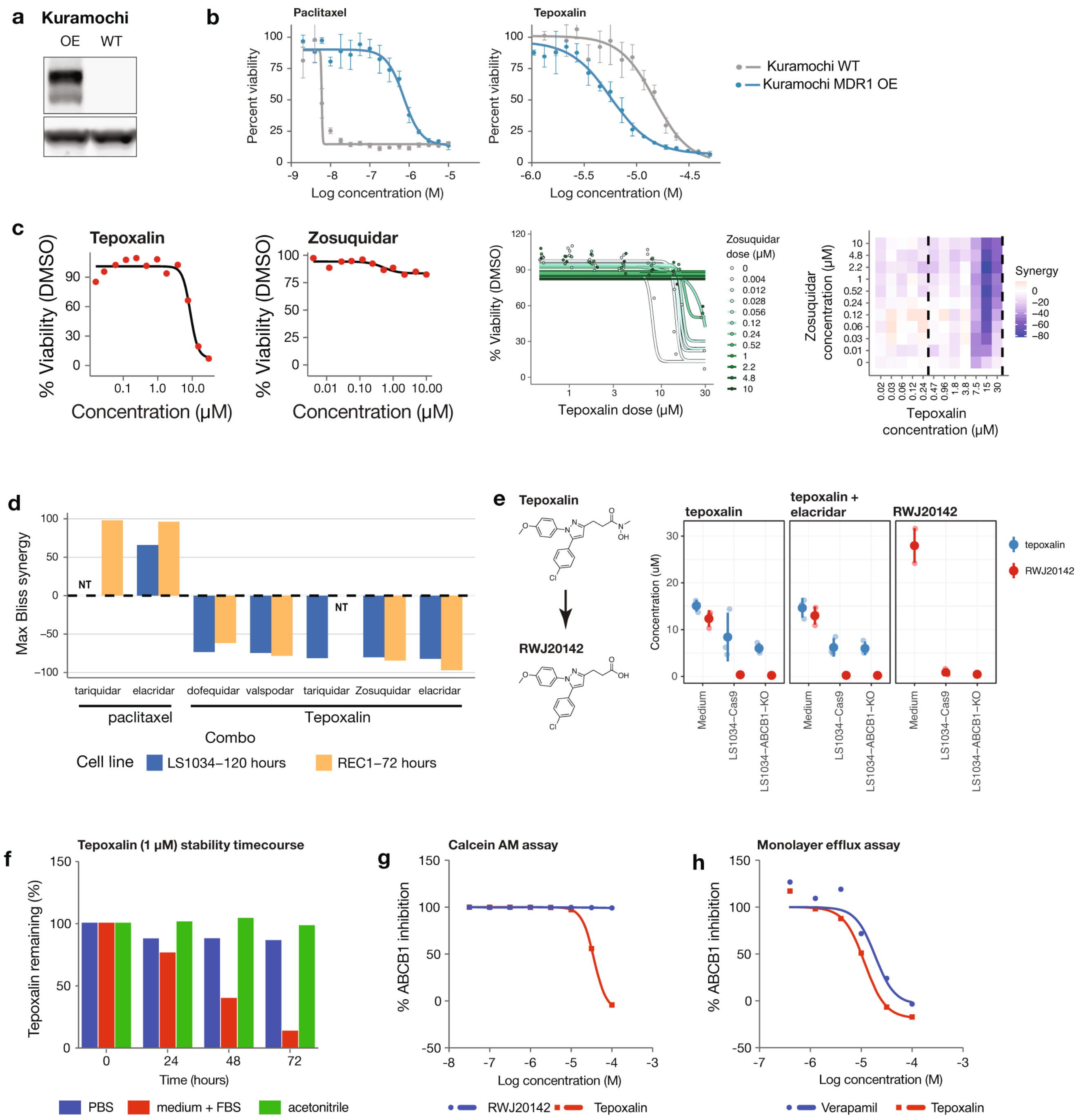

Extended Data Fig. 8 | Tepoxalin mechanistic studies. a, ABCB1 western blot with and without overexpression of ABCB1 in the Kuramochi ovarian cancer cell line. Western blot was performed once with three independent samples. **b**, Cellular viability of Kuramochi wild type and ABCB1-overexpressing cells after treatment with tepoxalin for 8 days. Mean viability across 3 independently treated wells is shown, with standard deviation indicated by error bars. **c**, (Left) Single-agent dose-response curves for LS1034 cells treated with tepoxalin and zosuquidar for 5 days. Two replicates were averaged. (Middle) Dose response curves for tepoxalin in combination with varying doses of zosuquidar (indicated by different colors) for 5 days. Data are shown for tepoxalin doses above 470 nM (the range indicated by the vertical dashed lines above). (Right) Bliss synergy scores estimated for each dose combination, showing strong antagonism by zosuquidar at tepoxalin doses above ~5 μM. Two combinations were not tested (NT). **d**, Maximum synergy score is shown across several drug combinations measured in both LS1034 and REC1 cell lines. Both tariquidar and elacridar were strongly synergistic in combination with paclitaxel, while all MDR1 inhibitors tested were antagonistic in combination with tepoxalin. **e**, Cellular permeability study of tepoxalin and RWJ20142 in LS1034 colon cancer cell lines with and without ABCB1 knockout. Each indicated cell line or media-only control was treated with 20 μM tepoxalin or RWJ20142 for 3 hours. Tepoxalin and RWJ20142 concentrations in cell lysate or medium were determined by liquid chromatography-mass spectrometry. Mean viability across 3 independently treated wells is shown, with standard deviation indicated by error bars. Shaded dots indicate underlying data. **f**, Stability study of tepoxalin in three different vehicles over 72 hours. Percent of tepoxalin remaining is indicated at each timepoint. **g**, ABCB1 antagonism assay using calcein AM fluorescence. MDCKII cells were treated with indicated concentration of tepoxalin or RWJ20142. Mean percent ABCB1 inhibition across 3 replicates is shown. **h**, ABCB1 transport-based activity assay. Basolateral transport of the ABCB1 substrate loperamide was assessed using a monolayer of MDCK-ABCB1 cells in the presence of tepoxalin or RWJ20142. Mean percent ABCB1 inhibition across 2 replicates is shown.

nature research

Corresponding author(s): Todd R. Golub

Last updated by author(s): Nov 21, 2019

Reporting Summary

Nature Research wishes to improve the reproducibility of the work that we publish. This form provides structure for consistency and transparency in reporting. For further information on Nature Research policies, see Authors & Referees and the Editorial Policy Checklist.

Statistics

For all statistical analyses, confirm that the following items are present in the figure legend, table legend, main text, or Methods section.

n/a	Confirmed	
☐	☒	The exact sample size (n) for each experimental group/condition, given as a discrete number and unit of measurement
☐	☒	A statement on whether measurements were taken from distinct samples or whether the same sample was measured repeatedly
☐	☒	The statistical test(s) used AND whether they are one- or two-sided *Only common tests should be described solely by name; describe more complex techniques in the Methods section.*
☐	☒	A description of all covariates tested
☐	☒	A description of any assumptions or corrections, such as tests of normality and adjustment for multiple comparisons
☐	☒	A full description of the statistical parameters including central tendency (e.g. means) or other basic estimates (e.g. regression coefficient) AND variation (e.g. standard deviation) or associated estimates of uncertainty (e.g. confidence intervals)
☐	☒	For null hypothesis testing, the test statistic (e.g. F, t, r) with confidence intervals, effect sizes, degrees of freedom and P value noted *Give P values as exact values whenever suitable.*
☒	☐	For Bayesian analysis, information on the choice of priors and Markov chain Monte Carlo settings
☒	☐	For hierarchical and complex designs, identification of the appropriate level for tests and full reporting of outcomes
☐	☒	Estimates of effect sizes (e.g. Cohen's d, Pearson's r), indicating how they were calculated

Our web collection on statistics for biologists contains articles on many of the points above.

Software and code

Policy information about availability of computer code

Data collection	Luminex xPONENT version 4.2 was used to collect data.
Data analysis	Data analysis was performed in R version 3.5.1. using custom or publicly-available R packages. Individual packages are explicitly cited in the manuscript and listed below. The custom code is available upon request and from GitHub (https://github.com/broadinstitute/repurposing). Graphpad PRISM version 8 was used for curve fitting and dose response plots. The following software packages were used for data analysis: DESeq2 v3.10 Limma v3.38.3 Atlantis (cancerdatasci/atlantis SHA: 167fc0a338fc2686a27463eb55546f6e316d91b0 on github) MAGeCK v0.5 sva 3.30.1

For manuscripts utilizing custom algorithms or software that are central to the research but not yet described in published literature, software must be made available to editors/reviewers. We strongly encourage code deposition in a community repository (e.g. GitHub). See the Nature Research guidelines for submitting code & software for further information.

Data

Policy information about availability of data

All manuscripts must include a data availability statement. This statement should provide the following information, where applicable:

- Accession codes, unique identifiers, or web links for publicly available datasets
- A list of figures that have associated raw data
- A description of any restrictions on data availability

Raw and processed PRISM viability data are available from the Cancer Dependency Map portal (https://depmap.org/repurposing) and archived via Figshare (doi:10.6084/m9.figshare.9393293). An interactive version of Figure 2a and Figure 4 (with accompanying raw data) is also available on the Cancer Dependency Map portal; scatter plot source data is also deposited in Figshare (doi:10.6084/m9.figshare.9393293). The cell line features used for biomarker analysis are listed in Supplementary Table 10 and also archived via Figshare (doi:10.6084/m9.figshare.10277810). RNA sequencing data were deposited in the Gene Expression Omnibus (GEO, accession number GSE133299). All other data supporting the findings of this study are available from the corresponding author on reasonable request.

Field-specific reporting

Please select the one below that is the best fit for your research. If you are not sure, read the appropriate sections before making your selection.

☒ Life sciences ☐ Behavioural & social sciences ☐ Ecological, evolutionary & environmental sciences

For a reference copy of the document with all sections, see nature.com/documents/nr-reporting-summary-flat.pdf

Life sciences study design

All studies must disclose on these points even when the disclosure is negative.

Sample size	No sample size calculation was performed. PRISM cell lines were selected based on ability to be transduced with lentivirus and adapt to shared culture conditions. In the primary screen, data was collected for 578 cell lines. 489 cell lines were included in the secondary screen based, in part, on primary screen QC performance. The 578 cell line panel spans a range of multiple cancer types, patient age (pediatric and adult cancer lines), and gender.
Data exclusions	A standardized QC process was employed for the processing of PRISM data. The rationale for filtering data was to remove low quality data points due to technical failures. Replicate-level outliers were filtered using the approach fully described in Methods and Extended Data Fig. 2-4. All filtered data is still included in the raw data files.
Replication	The PRISM screen was performed with 3 independently treated well replicates. Multiple independent cell treatments were performed for confirmatory studies as indicated in the Methods. Results shown are indicative of multiple independent experiments as indicated in the figure legends.
Randomization	All cell lines were tested with active treatments and a vehicle control. No individual experimental groups were used that would necessitate a randomized design.
Blinding	PRISM data was generated without the investigators' knowledge of compound and cell line identities during screening. Investigators were not blind to compound and cell line identities during analysis in order to interpret results within the context of known drug activities.

Reporting for specific materials, systems and methods

We require information from authors about some types of materials, experimental systems and methods used in many studies. Here, indicate whether each material, system or method listed is relevant to your study. If you are not sure if a list item applies to your research, read the appropriate section before selecting a response.

Materials & experimental systems

n/a	Involved in the study
☐	☒ Antibodies
☐	☒ Eukaryotic cell lines
☒	☐ Palaeontology
☒	☐ Animals and other organisms
☒	☐ Human research participants
☒	☐ Clinical data

Methods

n/a	Involved in the study
☒	☐ ChIP-seq
☒	☐ Flow cytometry
☒	☐ MRI-based neuroimaging

Antibodies

Antibodies used	The following antibodies were used: polyclonal rabbit anti-PDE3A from Bethyl Laboratory (A302-740A, 1:1000 dilution), monoclonal mouse anti-V5 from Life Technologies (R960-25, 1:5000 dilution), monoclonal rabbit anti-ABCB1 (D3H1Q) from Cell Signaling Technology (12683, 1:1000 dilution), monoclonal mouse anti-β-Actin (8H10D10) from Cell Signaling Technology (3700, 1:1000 dilution) , and monoclonal rabbit anti-SLC26A2 Antibody (3F6) from Novus Biologicals (H00001836-M04, 1:1000 dilution).
Validation	We validated the ABCB1 and SLC26A2 antibodies by performing gene knockout by CRISPR/Cas9 as reported in this manuscript. For the anti-V5 antibody, the manufacturer provides western blot validation by expressing a V5-tagged transgene. For the PDE3A antibody, IP validation is available from the manufacturer and in the literature (PMID26656089). The actin antibody has validation western blot data available from the manufacturer and is widely cited in the literature.

Eukaryotic cell lines

Policy information about cell lines

Cell line source(s)	Parental cell lines were obtained from the Broad-Novartis Cancer Cell Line Encyclopedia (CCLE) project prior to PRISM barcoding (see https://portals.broadinstitute.org/ccle for original sources). For follow-up studies, LS1034, HeLa, HEK293T cells were purchased from the American Type Culture Collection. REC1, SF295, OVISE, COLO320, BEN, HT29 and SNU449 were provided by CCLE. Wildtype and ABCB1 overexpressing (pLX_317 vector) Kuramochi cell lines were gifts from Elizabeth Stover (PMID31462500). HeLa PDE3A CRISPR KO cells (PDE3A-/- cells) were previously described (PMID26656089). LS1034, SF295, A2058, COLO320, SNU449 and OVISE cell lines derived with Cas9 were provided by the Broad Cancer Dependency Map.
Authentication	STR fingerprinting was performed by Genetica using the PowerPlex® 16 HS system (Promega). STR profiles were compared with STR profiles reported by vendors and in literature. Misidentified cell lines or other STR conflicts are listed in Supplementary Table 9. These cell lines are flagged in the data files and are not shown by default in the website interface.
Mycoplasma contamination	All cell lines tested negative for mycoplasma contamination.
Commonly misidentified lines (See ICLAC register)	KPL-1/MCF-7 and NCI-2077/NCI-H1581 have been listed in ICLAC as misidentified or derivative lines.